PAPER • OPEN ACCESS

Peripheral temperature gradient screening of high-Z impurities in optimised 'hybrid' scenario H-mode plasmas in JET-ILW

To cite this article: A.R. Field *et al* 2023 *Nucl. Fusion* **63** 016028

View the article online for updates and enhancements.

Peripheral temperature gradient screening of high-Z impurities in optimised 'hybrid' scenario H-mode plasmas in JET-ILW

A.R. Field[1,*] , **F.J. Casson**[1] , **D. Fajardo**[2] , **C. Angioni**[2] , **C.D. Challis**[1], **J. Hobirk**[2] ,
A. Kappatou[2] , **Hyun-Tae Kim**[1], **E. Lerche**[1,3], **A. Loarte**[4] , **J. Mailloux**[1]
and JET Contributors[a]

[1] United Kingdom Atomic Energy Authority, Culham Centre for Fusion Energy, Culham Science Centre, Abingdon OX14 3DB, United Kingdom of Great Britain and Northern Ireland
[2] Max-Planck-Institut für Plasmaphysik, Boltzmannstrasse 2, D-58748 Garching, Germany
[3] LPP-ERM-KMS, EUROfusion Consortium Member, Trilateral Euregio Cluster, TEC partner, Brussels, Belgium
[4] ITER Organization, Route de Vinon sur Verdon, 13115 Saint Paul lez Durance, France

E-mail: anthony.field@ukaea.uk

CrossMark

Abstract

Screening of high-Z (W) impurities from the confined plasma by the temperature gradient at the plasma periphery of fusion-grade H-mode plasmas has been demonstrated in the JET-ILW (ITER-like wall) tokamak. Through careful optimisation of the hybrid-scenario, deuterium plasmas with sufficient heating power ($\gtrsim 32\,\mathrm{MW}$), high enough ion temperature gradients at the H-mode pedestal top can be achieved for the collisional, neo-classical convection of the W impurities to be directed outwards, expelling them from the confined plasma. Measurements of the W impurity fluxes between and during edge-localised modes (ELMs) based on fast bolometry measurements show that in such plasmas there is a net efflux (loss) between ELMs but that ELMs often allow some W back into the confined plasma. Provided steady, high-power heating is maintained, this mechanism allows such plasmas to sustain high performance, with an average D–D neutron rate of $\sim 3.2 \times 10^{16}\,\mathrm{s}^{-1}$ over a period of $\sim 3\,\mathrm{s}$, after an initial overshoot (equivalent to a D–T fusion power of $\sim 9.4\,\mathrm{MW}$), without an uncontrolled rise in W impurity radiation, giving added confidence that impurity screening by the pedestal may also occur in ITER, as has previously been predicted (Dux *et al* 2017 *Nucl. Mater. Energy* **12** 28–35).

---

[*] Author to whom any correspondence should be addressed.
[a] See Mailloux *et al* 2022 (https://doi.org/10.1088/1741-4326/ac47b4) for JET Contributors.

1. Introduction

The JET-ILW tokamak [1] has an all-metal (Be/W) first-wall, as is to be used in the ITER device [2], both to overcome the problem of tritium retention in graphite plasma facing materials (PFMs) and to handle the high stationary heat loads to the divertor targets [3]. A disadvantage with using high-Z (74) tungsten W as a target material is that W is not fully ionized, even in the plasma core at temperatures required for a burning D–T plasma ($\gtrsim 10$ keV) [4], as currently achieved in JET-ILW and expected in ITER. Such partially ionized W ions are able to radiate strongly [5] ($\gtrsim \mathcal{O}(10)$ more than other PFMs), hence cooling the core plasma and potentially leading to plasma disruptions. Furthermore, calculations show that for a W concentration of $C_W \gtrsim 1.9 \times 10^{-4}$, ignition of a fusion reactor is not possible [6].

Predictions for ITER have suggested that W contamination of the confined plasma can be avoided if the ion temperature at the top of the edge transport barrier (ETB), which forms the H-mode 'pedestal', is sufficiently high [7]. This so-called 'temperature-gradient screening' occurs when the ion temperature gradient $T_i' = dT_i/dr$ is sufficiently strong compared to the ion density gradient n_i' [8, 9], causing outward impurity convection to expel the impurities from the confined plasma.

Recent experiments on JET-ILW have demonstrated impurity screening by the temperature gradient at the pedestal for the first time in carefully optimised 'hybrid'-scenario H-mode deuterium (D) plasmas with sufficiently high, sustained heating power ($P_{in} \gtrsim 32$ MW) [10]. Such pulses can achieve a D–D neutron rate $\Gamma_{n,DD} \sim 3.2 \times 10^{16}$ n s^{-1}, which is an average over the period 8.5–11.5 s, after an initial overshoot (equivalent to a fusion power of ($P_{fus} \sim 9.1$ MW for a 50:50 D–T fuel mix) [11], without an uncontrolled rise in W impurity radiation, giving confidence that this impurity mitigation mechanism may occur in ITER.

Screening of W impurities from the core plasma also occurs in ITER-baseline scenario plasmas in JET-ILW, which operate at higher plasma current and safety factor q than hybrid scenario plasmas. In baseline plasmas, outward neo-classical (NC) convection localises the W impurities just inside the pedestal top, where they can be efficiently flushed by edge-localised modes (ELMs) [12]. Maintaining good confinement with control of W radiation requires moderate D$_2$ gas puffing and ELM pacing pellets to avoid disruptions induced by excess edge radiation [13]. ITER-baseline plasmas run at low or zero rates of D$_2$ gas fuelling, exhibiting small, high-frequency ELMs, also exhibit temperature-gradient screening at the pedestal top, which is enhanced by a hot, low collisionality pedestal and with Ne impurity seeding the level of W radiation can be controlled [14].

Here, we show how the initial D$_2$ gas fuelling during the early phase of hybrid-scenario pulses can be optimised to produce a hot, low-collisionality, strongly rotating plasma at the pedestal top, which screens the W impurities from the confined plasma. Recent, improved understanding of collisional, NC impurity transport [15–17] based on interpretation of drift-kinetic calculation results from the NEO code [18–20], has shown the temperature gradient screening to be enhanced at low collisionality and by strong toroidal flow (Mach numbers $M_{\phi,i} = R\Omega_\phi/v_{th,i} \sim \mathcal{O}(1)$, where Ω_ϕ is the toroidal rotation rate, $v_{th,i} = (2T_i/m_i)^{1/2}$ is the ion thermal velocity, $m_i = A_i m_p$ and $A_i = 2$ for the main D^+ ions)—conditions favoured by the initially low gas fuelling rate.

Data from analysis of fast, bolometric total radiation measurements [21] is used to measure changes in the relative W content of the core plasma occurring between and during ELMs, thereby quantifying the W fluences (i.e. time-integrated fluxes) due to impurity transport across the pedestal between and during ELMs. These measurements clearly show that the optimised, hot pedestal reduces and, on-average, reverses the flux of W crossing the pedestal between ELMs. These results are consistent with the presence of impurity screening from the confined plasma in these plasmas, in contrast to the case in ITER-baseline plasmas in JET-ILW, which rely on impurity flushing by ELMs to control the impurity radiation [12].

A less desirable consequence of the resulting low W density in the outer, 'mantle' region of the optimised plasma is that the ELMs no longer expel or 'flush' W but on-average, allow the W to re-enter the plasma from the surrounding scrape-off-layer (SOL). Such a reversal of ELM flushing of impurities, resulting from hollowing of the W impurity density profile across the pedestal by NC temperature-gradient screening, is predicted in [22] by means of modelling using a full-orbit particle extension to the non-linear MHD code JOREK [23].

The remainder of the paper is structured as follows: in section 2, parameters of the two hybrid scenario pulses are presented and key features of this operational scenario discussed. Details of how the startup phase of the pulse is optimised to achieve a hot pedestal are presented in section 2.1 and general features of the total radiation distribution in these pulses are discussed in section 2.2. The main results of experimental analysis and interpretive modelling are presented in the rather extensive section 3, which are first previewed in its introduction. Finally in section 4, the available evidence for peripheral W screening is summarised in section 4.1 and implications for ITER operation discussed in section 4.2.

2. Hybrid-scenario pulses

Two different ELMy H-mode scenarios are under preparation for high-power D–T operation in both JET-ILW [24] and ITER: the ITER-baseline scenario operating at a normalised

plasma pressure $\beta_N \sim 1.8\text{--}2$ [5] and low edge safety factor[6] $q_{95} \sim 3$ and the hybrid scenario with a lower ratio of plasma current I_p to toroidal field B_t and hence higher $\beta_N \sim 2\text{--}3$ and high $q_{95} \sim 5$ [25]. Hence, hybrid pulses operate with central q_0 at or just above 1, while baseline pulses have $q_0 < 1$ and hence exhibit saw-teeth instabilities of the plasma core. Another key difference in present experiments, is that the high I_p of baseline pulses favours a higher density at the H-mode pedestal top $n_{e,\text{ped}}$ [26] and hence a flatter, less peaked density profile than typical of hybrid pulses, in which the low-density pedestal is hotter and less collisional.

2.1. Startup optimisation

The evolution of two high-power $P_{\text{in}} \sim 32\text{--}35\,\text{MW}$ hybrid pulses, with $I_p/B_t = 2.2\,\&\,2.3\,\text{MA}/3.4\,\text{T}$ ($q_{95} \sim 4.8\text{--}5.0$) is compared in figure 1. The initial I_p ramp and timing of the heating power is tailored to produce a broad, flat q profile with $q_0 \gtrsim 1$, with the aim of avoiding deleterious MHD instabilities and allowing access to high β_N [29].

In the 2.2 MA pulse #96501, an initially high level of D_2 gas fuelling $\Gamma_{D_2} \sim 2 \times 10^{22}\,\text{e}\,\text{s}^{-1}$ induces an early transition to ELMy H-mode at $\sim 7.3\,\text{s}$, while the ion temperature at the top of the density pedestal $T_{i,\text{ped}}$ remains $\lesssim 1.3\,\text{keV}$. In the optimised 2.3 MA pulse #97781, this initial gas puff is delayed by $\sim 1\,\text{s}$, thereby delaying the density rise and the onset of the ELMs.

During the main heating phase in pulse #96501, divertor heat loads were mitigated using 4 Hz sweeping of the outer strike point radius, which was located close to the divertor cryopump. As part of the optimisation of pulse #97781, the sweeping frequency was increased to 20 Hz, with the strike point slightly further from the cryopump. This may have affected the ELM behaviour because the ELMs appear to be preferentially triggered during a specific phase of the sweep cycle and the outer strike-point location can affect the pumping behaviour.

A striking consequence of this delayed gas fuelling is to increase both $T_{i,\text{ped}}$ and the central $T_{i,0}$ particularly early in the pulse, just after the low-gas phase, when $T_{i,\text{ped}} \sim 2.5\,\text{keV}$. The concomitant increase in $T_{i,0}$ with $T_{i,\text{ped}}$ is partly a result of a degree 'stiffness' of the core heat transport, i.e. that the ion heat diffusivity χ_i increases above the threshold temperature gradient $R/L_{T_i,cr}$ required to destabilise ion-scale turbulence [30].

In the non-optimised pulse #96501, the radiated power $P_{\text{Rad}}^{\text{Pl}}$ quickly increases to $\sim 10\,\text{MW}$ by 7.9 s, representing a fraction $\mathcal{F}_{\text{Rad}}^{\text{Pl}} \sim 30\%$ of the heating power. Thereafter, $\mathcal{F}_{\text{Rad}}^{\text{Pl}}$ remains quite constant until 9.5 s when there is a temporary drop in the neutral beam injection (NBI) power, after which it increases to almost 50%. The significance of this observation is discussed later in section 3.4.
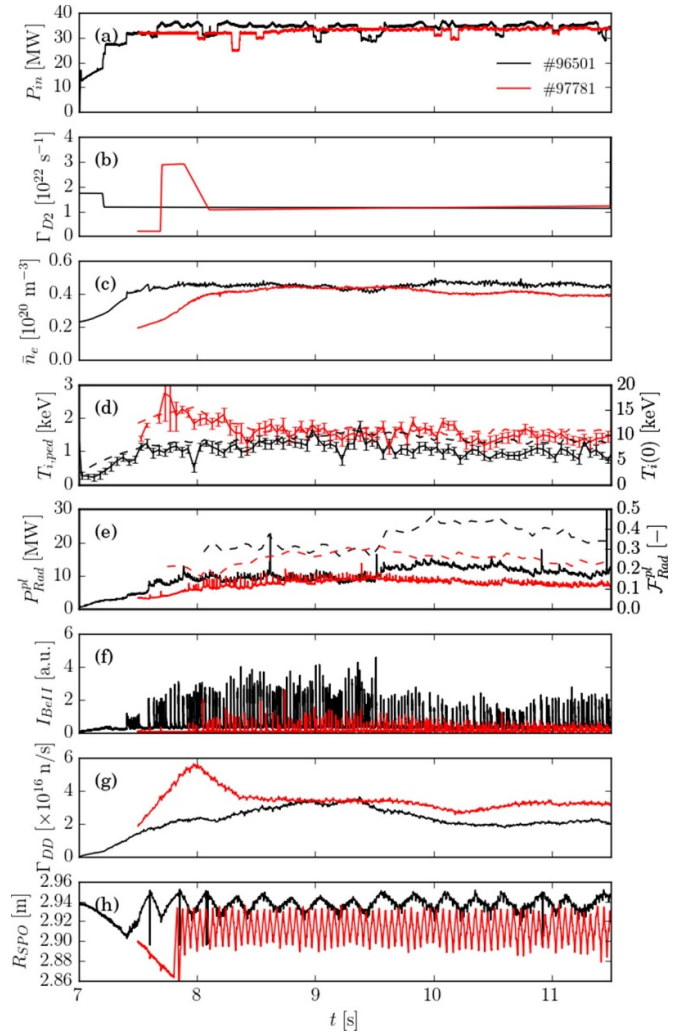
Figure 1. Comparison of the evolution of hybrid-scenario pulses #96501 and #97781 showing: (*a*) the total input power P_{in}; (*b*) the requested D_2 gas fuelling rate waveform Γ_{D_2} (does not include delays due to finite valve opening and gas transmission times or valve hysteresis effects); (*c*) the line-average density $\bar{n}_e$; (*d*) the ion temperature at the density pedestal top $T_{i,\text{ped}}$ measured by CXRS [27] (solid) and the central ion temperature $T_{i,0}$ measured by high-resolution spectroscopy of Ni^{+26} ions [28] (dashed); (*e*) the radiated power $P_{\text{Rad}}^{\text{Pl}}$ and radiated power fraction $\mathcal{F}_{\text{Rad}}^{\text{Pl}}$ (dashed) from the confined plasma; (*f*) the ELM behaviour from a visible Be II line intensity measured viewing the outer divertor target; (*g*) the D–D neutron rate $\Gamma_{n,\text{DD}}$; and (*h*) the major radius of the outer strike point R_{SPO}.

In contrast, in pulse #97781 with the optimised gas-fuelling, the onset of the ELMs is delayed by $\sim 0.7\,\text{s}$. During the initial ELM-free H-mode phase when $T_{i,\text{ped}}$ is high, $P_{\text{Rad}}^{\text{Pl}}$ is reduced by half, with $\mathcal{F}_{\text{Rad}}^{\text{Pl}} \sim 15\%$. After the onset of the ELMs, $P_{\text{Rad}}^{\text{Pl}}$ gradually increases, rising to the same level as in pulse #96501 by 9.5 s and then decreasing slightly after the W impurities accumulate in the plasma core.

As a consequence of the higher core ion temperature $T_{i,0}$, which primarily increases the thermal fusion rate coefficient $\langle\sigma_{\text{DD}}\rangle$, the D–D neutron rate $\Gamma_{n,\text{DD}}$ is more than twice as high in the optimised pulse than the non-optimised pulse, the
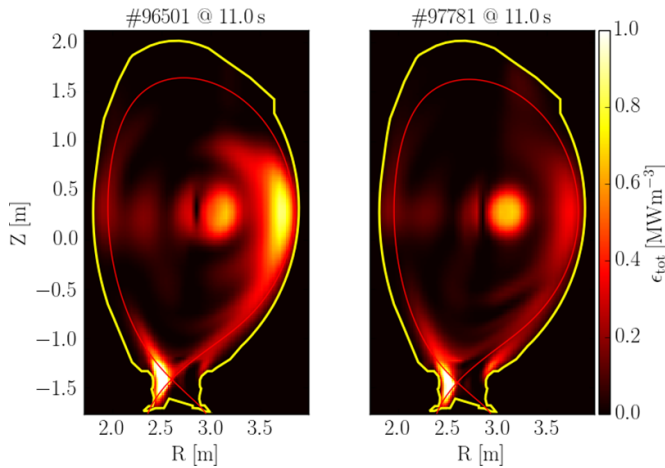
Figure 2. Comparison of the total radiated emissivity distributions $\epsilon_{\mathrm{tot}}(R,Z)$ from tomographic inversions of bolometric measurements for the two hybrid pulses #96501 (left) and #97781 (right) at 11 s, where outline of the first wall is shown in yellow and the separatrix contour in red.

fraction of thermal neutrons increasing from $\mathcal{F}_n^{\mathrm{th}} \sim 20\%$ to $\sim 50\%$ of the total rate.

2.2. Total radiation distribution

Distributions of the total radiated emissivity ϵ_{tot} at 11 s determined from tomographic inversions [31] of bolometric measurements are shown in figure 2 for the same two hybrid pulses. The radiation from the confined plasma is distinguished by two features: in a central region near the magnetic axis and another located around the outer plasma mid-plane in the outer third of the plasma radius, which we refer to here as the 'mantle' region[7]. Note that the radiation from the mantle is much weaker in the optimised than the non-optimised pulse, while the emissivity from the core region is similar.

There is also pronounced emission from the high-field-side (HFS) divertor region, reminiscent of the HFS high-density (HFSHD) region observed in several devices operated at high radiation fractions [32], which may play an important role in the ELM induced transport of impurities across the separatrix.

Analysis of such radiation distributions in high-power baseline pulses in JET-ILW [33] has shown that the radiated power is dominated by W, with these impurities typically emitting $\gtrsim 80\%$ of the total radiated power. The outwardly asymmetric poloidal emissivity distribution results from centrifugal forces on the heavy W ions due to the strong toroidal rotation driven by the tangentially oriented NBI heating [34]. The conclusion that W dominates the total radiation is supported by an integrated analysis of Z_{eff}, soft x-ray and total radiation measurements [35].

---

[7] The mantle region is defined here as $0.7 \leqslant \rho_{\mathrm{tor}} \leqslant 0.95$, where the normalised radial coordinate $\rho_{\mathrm{tor}} = \Phi_N^{1/2}$ and Φ_N is the normalised toroidal flux.

3. Cross-pedestal W fluxes

In this section, the main results of the experimental analysis and interpretive modelling are presented.

In section 3.1, the method of analysis used to determine the cross-pedestal W fluences (time integrated fluxes) from fast bolometric total radiation measurements, both during and between ELMs, is explained and then the results of this analysis are summarised in section 3.2. The W accumulation behaviour later in the steady, ELMy H-mode phase of these pulses is then discussed in section 3.3.

The 'ELM-flushing' data quantifies the W fluences entering/leaving the confined plasma across the pedestal region, in a manner which is independent of extensive modelling and shows that the 'normal' situation of W impurities entering the plasma between ELMs and being flushed out again by the ELMs is reversed in the later phase of the optimised pulse.

In order to better understand these observations, the collisional, NC convective fluxes of the W impurities across the pedestal and mantle regions are then discussed section 3.4, firstly introducing the necessary theoretical expressions in section 3.4.1 and then evaluating simplified proxies for the magnitude and strength of the NC convection in section 3.4.2. These are based on averaged values of the parameter $\zeta_{\mathrm{NC}} = R/2L_{T_i} - R/L_{n_i}$ (to which the NC convection velocity is proportional when the impurities are in the collisional PS regime).

Because of an uncertainty in the reliability of the charge-exchange recombination spectroscopic (CXRS) measurements across the pedestal gradient region, which are made on Ne^{10+} impurities rather than the main D^+ ions, the proxy for the NC convection ζ_{NC} and also the related parameter η_i (which, in the PS regime, has to exceed ~ 2 for an outward NC impurity flux, i.e. for $\zeta_{\mathrm{NC}} > 0$) are also calculated under the limiting assumption that $T_i = T_e$ across the pedestal region as the parameters $\langle \zeta_{\mathrm{NC},e} \rangle_{\mathrm{ped}}$ and $\langle \zeta_{\mathrm{NC},e} \rangle_{\mathrm{ped}}$.

The behaviour of these proxies for the NC convection, both averaged over the pedestal gradient region $\langle \zeta_{\mathrm{NC},i} \rangle_{\mathrm{ped}}$ and also its maximum value across the mantle region $\{\zeta_{\mathrm{NC},i}\}_{\mathrm{man}}^{\mathrm{max}}$ shows: (a) in both pulses the NC impurity convection is always outward across the mantle region, i.e. there is temperature gradient screening (b) using the measured T_i across the pedestal gradient region $\langle \zeta_{\mathrm{NC},i} \rangle_{\mathrm{ped}} \ll 0$, consistent with strong inward convection. However, under the assumption that $T_i = T_e$ across this region, this parameter reverses sign, i.e. $\langle \zeta_{\mathrm{NC},e} \rangle_{\mathrm{ped}} > 0$, consistent with impurity screening across the pedestal.

Evidence for hysteresis of the NC impurity screening, which appears as a consequence of a temporary reduction of NBI heating power in the non-optimised pulse, is presented in section 3.4.3, which shows that once the hot pedestal conditions are lost, impurities enter the plasma causing an irreversible change, from which the pulse does not recover.

The means to easily calculate this proxy $\zeta_{\mathrm{NC},i}$ for the NC convection across the pedestal and the mantle regions as a function of time from the Thompson scattering (TS) and CXRS profile measurements allows the inter-ELM

dynamics of the NC screening to be resolved, as presented in section 3.4.4.

Calculations of the NC W transport across the mantle region performed using NEO are presented section 3.5, which highlight the importance of enhancement of the magnitude of W screening across the mantle region by the stronger toroidal rotation at the pedestal top in the optimised pulse.

The kinetic profiles from the TS and CXRS measurements, which are used as input to these calculations, as well as those of the derived D^+ Mach number and collisionality, are presented in section 3.5.1, which also discusses in more detail the possible reasons why the CXRS measurements of T_i and $\Omega_{\phi,\text{ped}}$ may be unreliable in the pedestal gradient region.

The resulting transport coefficients of the W impurities from NEO calculations, which are performed both with and without toroidal rotation, are then presented in section 3.5.2, showing that both the NC diffusion and convection are strongly enhanced across the mantle region by the toroidal rotation, particularly in the optimise pulse.

As an experimental confirmation of these calculations, the resulting total emissivity profiles of the W impurities, which dominate the total radiated power in high-power JET-ILW pulses, are calculated as described in section 3.5.3 and compared with bolometric measurements in section 3.5.4.

Calculations using NEO of the NC W transport for a case where the input profiles are forced to give $T_i = T_e$ across the pedestal gradient region have not been performed because of the lack of direct measurements to support this hypothesis. Instead, the fact that the simplified proxy $\langle \zeta_{\text{NC},e} \rangle_{\text{ped}}$ is consistent with temperature gradient screening across the pedestal gradient region is considered as far as any proof of this conjecture can be taken here.

3.1. ELM W 'flushing' analysis

The fact that the total emissivity ϵ_{tot} is dominated by W in such pulses can be used to measure changes in the relative W content $\Delta \bar{n}_{\text{W}} / \bar{n}_{\text{W}}$ of the confined plasma due to ELMs and inter-ELM cross-pedestal particle transport, as described in [12]. This method [36] also relies on the fact that the cooling factor of W is relatively constant at $\mathcal{R}_\epsilon \sim 4.5 \times 10^{-13}$ W m^3 over temperature range prevailing over the mantle region, i.e. $1 \lesssim T_e \lesssim 2$ keV [37].

This, and the fact that the radiated power is proportional to n_e, i.e. $P_{\text{Rad}} \propto n_e \mathcal{R}_\epsilon n_{\text{W}}$, where n_{W} is the W density, can be availed of to determine relative changes in the W content using the relation $\Delta \bar{n}_{\text{W}} / \bar{n}_{\text{W}} \sim \Delta f_{\text{fl}} / f_{\text{fl}}$, where the 'flushing' signal $f_{\text{fl}} = P_{\text{Rad}}^{\text{man}} / \bar{n}_e$, where $P_{\text{Rad}}^{\text{man}}$ is the total radiation from the mantle region and $\bar{n}_e$ the line-averaged density measured along an interferometer chord through the mantle region [12]. Examples of the flushing signal f_{fl} and the derived, average W concentration over the mantle region $\langle C_{\text{W}} \rangle_{\text{man}}$, which is typically ~ 2–3×10^{-4}, are shown figure 3(a).

3.2. ELM and inter-ELM W fluences

Relative changes in the flushing signal f_{fl} over the intra-ELM and inter-ELM periods, which are $\mathcal{O}(1\,\text{ms})$ and

$\mathcal{O}(10$–$100\,\text{ms})$ in duration respectively, can be used to quantify relative changes in the W content $\Delta \bar{n}_{\text{W}} / \bar{n}_{\text{W}}$, due to the W fluences (i.e. the time-integrated fluxes) caused by the ELMs and transport across the pedestal between the ELMs respectively. Examples of such $\Delta \bar{n}_{\text{W}} / \bar{n}_{\text{W}}$ data are shown in figure 3(b), which also shows the net change over each ELM cycle. This data can also be used to determine rates of change of the W content Υ_{W} due to these processes, which are shown in figure 3(c) to be $\mathcal{O}(1$–$3\,\text{s}^{-1})$.

Average values of these relative changes in W content in the mantle region are stated in table 1 for the two pulses over time periods both during the initial phase of 7.5–9.0 s and later during the steady ELMy phase 9.5–12.0 s, after some impurities have migrated to the core. The data plotted in figure 3(b) from the post-accumulation phase is also plotted vs the relative ELM density losses $\Delta \bar{n}_e / \bar{n}_e$ in figures 4 and 5.

It can be seen from figure 3(b) that in the non-optimised pulse #96501, the ELMs typically flush out $\sim 7\%$ of the W from the mantle region, while a similar fraction then 'leaks' back into the confined plasma between the ELMs due to cross-pedestal transport. This is the typical situation when inward NC convection peaks the W impurity density in the pedestal region [22]. The net changes per-ELM cycle are consequently much smaller, which is consistent with the relatively steady W concentration and radiated power.

In contrast, in the optimised pulse #97781 with the higher $T_{i,\text{ped}}$, the typical magnitude of the changes in $\Delta \bar{n}_{\text{W}} / \bar{n}_{\text{W}}$ due both to the ELMs and inter-ELM transport are much smaller ($\lesssim 1\%$). However, on-average the situation is reversed, i.e. the inter-ELM transport expels W from the confined plasma, while the ELMs allow some W back into the plasma from the SOL.

This change in behaviour to a regime where the W impurity content is controlled by ELM flushing to a regime with peripheral impurity screening is illustrated clearly in figure 6. These observations are consistent with a hollow W impurity density in the pedestal region [22], due to the presence of NC temperature gradient screening across the pedestal.

3.3. W accumulation behaviour

The density profile of the heavy impurities n_Z is largely governed by the ratio of collisional, NC convection and diffusion [38]. If the impurities are in the collisional, Pfirsch–Schlüter (PS) regime, the stationary impurity density profile is related to that of the bulk D^+ ions n_i according to $n_Z/n_{z,0} = (n_i/n_{i,0})^Z (T_i/T_{i,0})^{-\frac{Z-1}{2}}$, i.e. a peaked density profile causes impurities to accumulate in the plasma core, while a peaked temperature opposes this, 'screening' out the impurities from the core.

For the W impurities, which typically have a mean charge in the core plasma of $\bar{Z} \sim 50$, if these accumulate, the impurity density peaking is extreme. The resulting radiation reduces the central electron temperature $T_{e,0}$, thereby modifying the current profile, quickly resulting in MHD instabilities and often plasma disruptions. For this reason, minority ion-cyclotron-resonance heating is used to inhibit full accumulation of the heavy impurities by modifying both the background plasma profiles and transport in the core [39, 40].
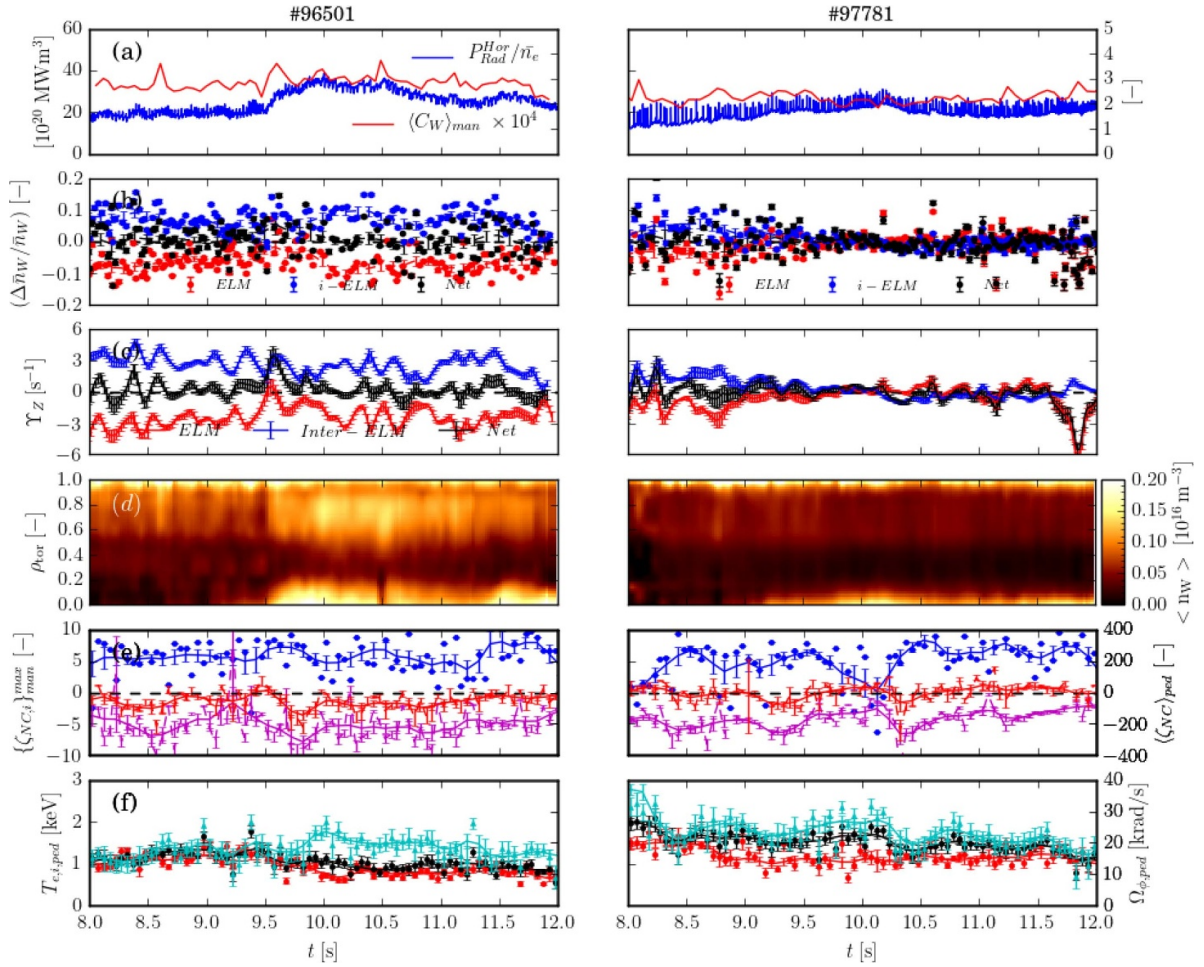
Figure 3. Evolution of hybrid-scenario pulses #96501 (left) and #97781 (right) showing: (*a*) the flushing signal $f_{fl} = P_{Rad}^{Pl}/\bar{n}_e$ (blue) and the mean W concentration over the 'mantle' region $\langle C_W \rangle_{man}$ (red); (*b*) relative changes in the W content of the confined plasma $\Delta\bar{n}_W/\bar{n}_W$ due to ELMs (•) and during the inter-ELM periods (•) and the net change over the ELM cycle (•); (*c*) the net rate of change of the W content Υ_W (black) and that due to ELMs (red), the inter-ELM transport (blue); (*d*) the FSA W density $\langle n_W \rangle$ as a function of normalized radius ρ_{tor}; (*e*) the parameter $\zeta_{NC} = R/2L_{T_i} - R/L_{n_i}$ calculated using the measured T_i profile averaged over the pedestal region $\langle \zeta_{NC,i} \rangle_{ped}$ (•) and its maximum value over the mantle region $\{\zeta_{NC,i}\}_{man}^{max}$ (•) (for comparison $\langle \zeta_{NC,e} \rangle_{ped}$, calculated assuming $T_i = T_e$ is also shown (•)); and (*f*) the toroidal rotation at the density pedestal top $\Omega_{\phi,ped}$ (•) and the pedestal temperatures $T_{e,ped}$ (•) and $T_{i,ped}$ (•).

Table 1. Relative changes W content per ELM $((\Delta\bar{n}_W/\bar{n}_W)_{ELM})$ and inter-ELM period $((\Delta\bar{n}_W/\bar{n}_W)_{i-ELM})$ for the two hybrid pulses shown in figure 3 averaged over the stated time periods.

Pulse	$(\Delta\bar{n}_W/\bar{n}_W)_{ELM}$		$(\Delta\bar{n}_W/\bar{n}_W)_{i-ELM}$	
#	(%)		(%)	
$t_0 - t_1$	7.5–9.5 s	9.5–11.5 s	7.5–9.5 s	9.5–11.5 s
96501	-7.1 ± 0.3	-6.7 ± 0.4	7.4 ± 0.4	7.0 ± 0.5
97781	-3.1 ± 0.6	0.4 ± 0.1	3.1 ± 0.5	-0.7 ± 0.1

Because W dominates the total emissivity, its approximate flux-surface-averaged (FSA) density can be calculated from $\langle n_W \rangle \sim \epsilon_{tot}/(\mathcal{R}_\epsilon n_e)$, as shown for the two hybrid pulses in figure 3(*d*). During these pulses, there a gradual peaking of the ion density profile n_i with respect to the T_i profile, which, combined with profile changes caused by MHD islands [41], triggers reversal of the NC convection, causing the W to accumulate in the plasma core after ~9.3 s. However, the central

W concentration remains low enough not to cause intolerable T_e profile hollowing. Note that in the optimised pulse #97781, the W content is about half that in the non-optimised pulse #96501, with about a factor ~×2 less in the outer mantle region of the plasma.

3.4. Collisional, NC impurity flux

3.4.1. Theoretical expressions. The flux of impurity ions denoted with the subscript I of charge state Z averaged over a flux surface is given by $\langle \Gamma_I \cdot \nabla r \rangle = \langle n_I V_I \rangle$, where n_I is its density and V_I is the radial convective velocity. When the main ions are in the collisionless, 'banana' regime and the impurity ions are in the collisional, PS regime and uniformly distributed over a flux surface, i.e. centrifugal effects due to toroidal rotation are negligible ($M_\phi \ll 1$), the impurity convection velocity $V_I^{PS} = \langle \Gamma_I \cdot \nabla r \rangle / \langle n_I \rangle$ is given by equation 12 of [42]:

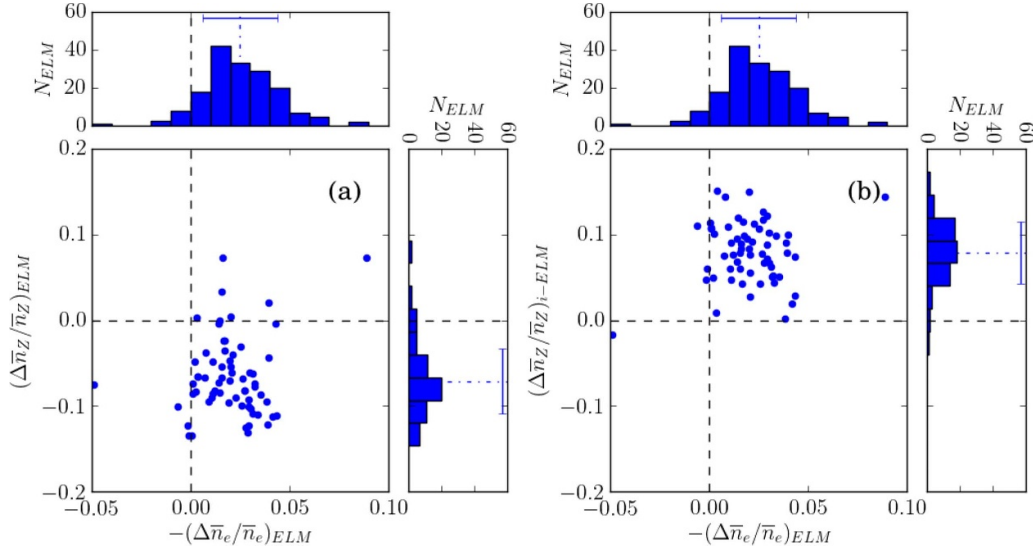$$V_I^{PS} = 2q^2 D_c Z [C_{TS}/L_{T_i} - 1/L_{n_i}] \qquad (1)$$

Figure 4. The relative W content flushed by the ELMs $(\Delta \bar{n}_{\mathrm{W}}/\bar{n}_{\mathrm{W}})_{\mathrm{ELM}}$ (*a*) and the relative inter-ELM influx $(\Delta \bar{n}_{\mathrm{W}}/\bar{n}_{\mathrm{W}})_{i-\mathrm{ELM}}$ (*b*) vs the relative ELM density losses $-\Delta \bar{n}_e/\bar{n}_e$ for pulse #96501 during the post-accumulation phase over the time period 9.5–11.5 s, where the histograms show the amplitude distribution on both axes, with average and standard deviations indicated by the error bars.
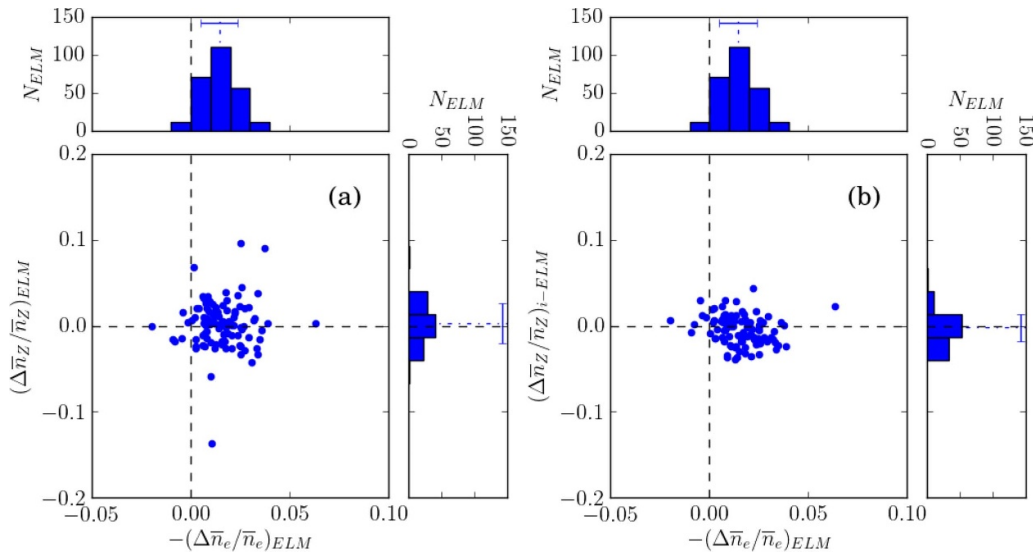

Figure 5. As figure 4 for pulse #97781.

where the classical, collisional diffusion coefficient $D_c = \rho_i^2/\tau_{ii}$ and τ_{ii} is the self collision time of the bulk ions[8], the 'temperature screening' coefficient $C_{\mathrm{TS}} = 1/2$ [8] and the scale lengths are defined as, e.g. $L_{n_i} = -\partial \ln n_i/\partial r$, i.e. positive for a peaked profile. Hence, the density gradient drives the impurities inwards causing them to accumulate in the plasma core, while the T_i gradient acts to inhibit this accumulation.

Note that a corollary of equation (1) is that the condition for temperature screening of the impurities ($V_I^{\mathrm{PS}} > 0$) in the PS regime is for the parameter $\eta_i = L_{n_i}/L_{T_i}$ to exceed the critical value $\eta_{i,cr} = 1/C_{\mathrm{TS}} \sim 2$.

For convenience, we define the bracketed term as a proxy for the NC convection as $\zeta_{\mathrm{NC}} = C_{\mathrm{TS}}(R/L_{T_i}) - R/L_{n_i}$, which is simple to calculate to give an approximate estimate of the strength of the impurity convection, such that $V_Z = 2q^2 D_c Z\zeta_{\mathrm{NC}}/R$. Typically, the W ions are in charge states W^{25-30+} in the mantle region [33], so this convection is very strong for the W ions.

In the case of strong toroidal rotation ($M_\phi \sim \mathcal{O}(1)$), e.g. as driven by tangential NBI heating, centrifugal effects localise the heavy impurities such as W ($m_Z/m_p = 184$) to the outboard low-field side (LFS) mid-plane of the plasma. These effects are treated for the case of the heavy impurities in the PS regime in [42], in which it is shown that with strong localisation, the impurity fluxes are enhanced by the factor $1/2\epsilon^2$, where the inverse aspect ratio $\epsilon = r/R$, i.e. by a factor ~5 for the peripheral region of JET-ILW.

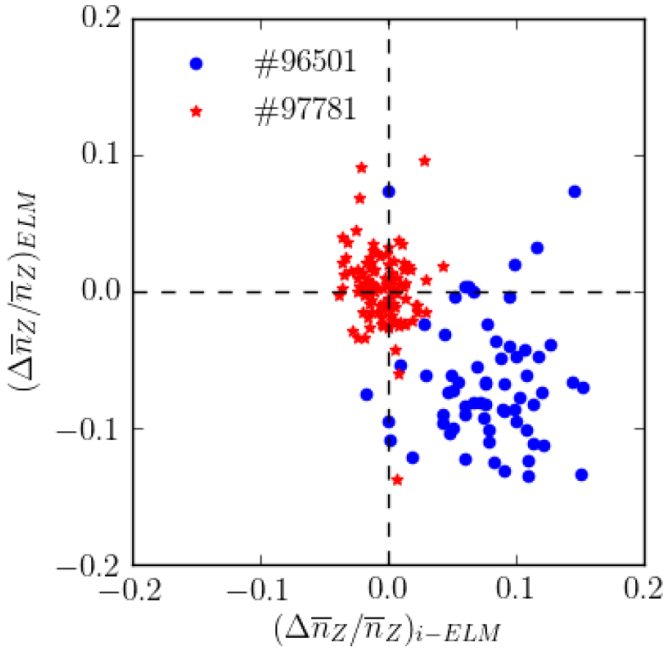---

[8] The self-collision time of the hydrogenic main ions is defined as $\tau_{ii} = \frac{3(2\pi)^{3/2}\epsilon^2\sqrt{m_p}T_i^{3/2}}{n_i e^4 \ln \Lambda}$, where m_p is the proton mass and $\ln \Lambda$ is the Coulomb logarithm [43].

Figure 6. A comparison of the relative changes in the W content of the plasma due to ELM flushing $(\Delta \bar{n}_W / \bar{n}_W)_{ELM}$ vs the change due to the inter-ELM influx $(\Delta \bar{n}_W / \bar{n}_W)_{i-ELM}$ between the non-optimised pulse #96501 and the optimised pulse #97781 for the time period 9.5–11.5 s, showing the change from ELM flushing to peripheral screening behaviour.

For the core plasma parameters achieved in these high-power hybrid-scenario pulses in JET-ILW, i.e. relatively low density and high temperature, the impurity ions are also in the banana regime. Under these conditions, a more complete treatment of NC theory for arbitrary collisionality regimes is required.

A convenient analytic form for the NC transport coefficients is derived in [15], which provides an approximation to results of the drift-kinetic code NEO [18], encompassing scans over the relevant parameter space. A general form for the impurity flux components $\langle \Gamma_I^c \rangle$ is given by equation 2 of [15]:

$$\frac{\langle \Gamma_I^c \rangle}{\langle n_I \rangle} = \frac{D_I^c}{L_{n_I}} - \frac{H_I^c}{L_{T_i}} - \frac{K_I^c}{L_{n_i}} \equiv V_I^c \qquad (2)$$

where the superscript c denotes the component due to classical (CL), PS and banana-plateau (BP) transport processes and V_I^c is the convection velocity. Both diffusion D_I^c and convection K_I^c coefficients are positive, hence, for normal, peaked profiles ($L > 1$), the diffusive flux is outward and the convective flux inward. However, because $D_I^c = K_I^c / Z_I$, the dominant, friction driven convection is inward [15].

The coefficients D_I^c, K_I^c, H_I^c in equation (2) are each dependent on the parameters (g, Z_I, A_I, f_t), where $g = qR/(v_{th,i}\tau_{ii}) \equiv \nu_{ii}^* \epsilon^{3/2}$ is the collisionality parameter and ν_{ii}^* is the main ion collisionality. Note that the ions are in the banana or PS regimes when $g < \epsilon^{3/2}$ and $g > 1$ (or $\nu_{ii}^* < 1$ and $\nu_{ii}^* > \epsilon^{-3/2}$) respectively—at the periphery of JET-ILW plasmas, $\epsilon^{3/2} \sim 0.15$.

Note that the convection coefficients H_I and K_I are both linearly proportional to the diffusion coefficient D_I in all collisionality regimes, so the total convection driven impurity flux (and hence its net radial convection velocity V_I) increases with D_I. However, the temperature screening parameter $C_{TS} = -H_I/K_I$ (where H_I and K_I are sums over each of the components, index c), is independent of the magnitude of D_I.

3.4.2. Estimates of strength and direction of NC convection. To give an approximate estimate of the strength and direction of the NC impurity convection, the spatial average of the convection parameter ζ_{NC}, calculated over the pedestal region and its maximum value over the mantle region are shown in figure 3(*e*), i.e. $\langle \zeta_{NC} \rangle_{ped}$ and $\{\zeta_{NC,i}\}_{man}^{max}$ respectively. For calculation of ζ_{NC}, T_i data from only the edge charge-exchange-recombination spectrometer system [27] is used and we assume $n_i = n_e$, where the n_e profile is measured by the high-resolution Thomson scattering system [44].

To implement this analysis, profiles of the quantities η_i and $\zeta_{NC,i}$, which require combining fitted T_i and n_e profile data, are first calculated by finding the closest CXRS data point to each of the TS pulses. Hence, the detailed behaviour of these quantities is approximate on timescales below 5 ms, i.e. half of the integration period of the CXRS measurements. Also, the values for $\Delta t_{ELM} < 5$ ms may be affected by the influence of the ELM on the CXRS data.

Because the pedestal width $\Delta_{ped} \sim \mathcal{O}(2 \text{ cm})$ is of the order of the ion banana orbit width, i.e. the gyro-radius of the ions $\rho_{i,\theta}$ in the poloidal magnetic field B_p, it is appropriate to consider spatially averaged values of ζ_{NC} (or η_i) in the pedestal region. However, as the extent of the mantle region is $\mathcal{O}(10)$ larger, it is more appropriate to consider the maximum value of the screening parameters in this region. The corresponding values of ζ_{NC} and $\eta_{i,e}$ for the pedestal and mantle regions, averaged over time ranges before and after the W impurities accumulate in the plasma core at ~ 9.5 s are stated in table 2.

3.4.2.1. Mantle region. Throughout both of the pulses, the maximum value of ζ_{NC} across the mantle region is maintained at $\{\zeta_{NC,i}\}_{man}^{max} \sim 5$, i.e. the NC impurity convection is directed outwards, localising the W impurities to this region, where they can be efficiently flushed from the confined plasma by the ELMs.

Results of more accurate calculations of the NC convection in these pulses, performed numerically using the NEO code [18] presented in section 3.5, show that the strong enhancement due to the toroidal rotation in these pulses reveals marked differences in the NC convection between the two pulses, particularly in the mantle region, just inside the pedestal top.

3.4.2.2. Pedestal region. Two sets of data for ζ_{NC} averaged over the pedestal region are shown in figure 3(*e*) to give an indication of the possible range of values: $\langle \zeta_{NC,e} \rangle_{ped}$ calculated assuming $T_i = T_e$ and $\langle \zeta_{NC,i} \rangle_{ped}$ calculated using the T_i profile from CXRS.

Table 2. Time-averaged values over the specified time ranges of the spatially averaged values $\langle\ldots\rangle$ of $\zeta_{NC,i/e}$ and $\eta_{i/e}$ for the pedestal region and $\{\ldots\}^{max}$ values of ζ_{NC} and η_i over the mantle region, where the two values for the pedestal region are calculated using the measured T_i and assuming $T_i = T_e$.

Pulse	$\langle\zeta_{NC,i}\rangle_{ped}$		$\langle\zeta_{NC,e}\rangle_{ped}$		$\{\zeta_{NC,i}\}^{max}_{man}$	
#	$t_0 - t_1 = 7.5\text{–}9.5\,s$	9.5–11.5 s	7.5–9.5 s	9.5–11.5 s	7.5–9.5 s	9.5–11.5 s
96501	-134 ± 11	-77 ± 11	-15 ± 9	-41 ± 7	5.6 ± 0.4	5.9 ± 0.5
97781	-124 ± 12	-78 ± 8	$+11 \pm 10$	$+51 \pm 8$	5.0 ± 0.4	5.5 ± 0.6

—	$\langle\eta_i\rangle_{ped}$		$\langle\eta_e\rangle_{ped}$		$\{\eta_i\}^{max}_{man}$	
#	7.5–9.5 s	9.5–11.5 s	7.5–9.5 s	9.5–11.5 s	7.5–9.5 s	9.5–11.5 s
96501	-0.35 ± 0.3	0.28 ± 0.03	1.8 ± 0.08	1.9 ± 0.06	3.8 ± 0.2	5.4 ± 0.5
97781	-0.34 ± 0.2	0.50 ± 0.03	2.1 ± 0.05	2.6 ± 0.10	3.9 ± 0.3	3.9 ± 0.2

For the non-optimised pulse #96501, both estimates of $\langle\zeta_{NC}\rangle_{ped}$ are consistent with strong inward NC impurity convection across the pedestal between ELMs, i.e. $\langle\zeta_{NC}\rangle_{ped} \ll 0$, albeit reduced in magnitude assuming $T_i = T_e$. For the optimised pulse #97781, the average value of $\langle\zeta_{NC,i}\rangle_{ped} \sim \mathcal{O}(-100)$, is also consistent with strong inward W convection across the pedestal. However, the estimate made assuming $T_i = T_e$ of $\langle\zeta_{NC,e}\rangle_{ped} \sim +11$ in the initial phase and $+50$ after 9.5 s, implies screening of the W impurities by the pedestal temperature gradient. This arises due to a change, from the non-optimised to the optimised pulse, in η_i (assuming here $\eta_i \equiv \eta_e$) across the pedestal to a value exceeding the critical value $\eta_{i,cr} \sim 2$ required for outward NC convection.

On devices with a main ion (D^+) CXRS system, e.g. DIII-D, it is often found that over the pedestal region the ion-temperature gradient T_i' is closer to T_e' than that measured on the impurity ions (i.e. C^{6+} on DIII-D or Ne^{10+} on JET-ILW) [45]. As there are no measurements of the main D^+ ion temperature on JET-ILW, these estimates of ζ_{NC} made assuming $T_i = T_e$ are purely conjectural and offer an alternative explanation of the observations of (a): controlled W impurity radiation, particularly from the mantle region in the optimised pulse #97781; and (b) the apparent reversal of the flushing behaviour of the ELMs in this pulse after 9.5 s, when magnitude of $\langle\zeta_{NC,e}\rangle_{ped}\,(>0)$ is larger; to that offered by the more comprehensive calculations of the W convection presented in section 3.5 below.

The maximum sustainable difference between temperatures of impurity ions and the main ion species due to collisional equipartition has been investigated in [46]. This steady-state analysis is appropriate for the case when the collisional equipartition time τ_{Zi} between the impurities and main ions is much shorter than the energy confinement time, i.e. $\tau_{Zi}/\tau_{E,th} \ll 1$, as is the case in the core plasma. However, in the pedestal region the local confinement time of the impurity ions is much shorter and may be comparable or shorter than τ_{Zi}, allowing larger temperature differences to be sustained at the plasma periphery than in the core.

As mentioned in section 2.1, the reduced early gas fuelling in pulse #97781 more than doubles the initial pedestal ion temperature at the pedestal top $T_{i,ped}$ compared to that in pulse #96501, which remains higher throughout the pulse. As also shown in figure 3(*f*), the reduced early gas fuelling results in an even greater increase in the toroidal rotation rate at the pedestal top $\Omega_{\phi,ped}$ early on in the pulse, initially by a factor ~ 3, although this enhancement decreases later on when the fuelling rates are the same. Note that the pedestal top density $n_{e,ped} \sim 0.3 \times 10^{20}\,m^{-3}$ remains quite constant throughout the sustained phase of both pulses.

3.4.3. Hysteresis of impurity screening. The evolution of the ELM frequency f_{ELM}, the normalised density and temperature gradients and the parameters $\eta_{i,e}$ across the pedestal in the non-optimised pulse #96501 and optimised pulse #97781 are shown in figure 7. After ~ 9.5 s when the W accumulates in the plasma core, there is a difference in the behaviour of f_{ELM} between the two pulses, i.e. in pulse #96501 f_{ELM} decreases, while in #97781 f_{ELM} increases compared to that in the earlier phase, when it is similar in both pulses. The cause of these changes in f_{ELM} can be explained by the behaviour of the radiated power fraction $\mathcal{F}_{Rad}$ (see figure 1(*e*) and related discussion in section 2.1) in terms of the resulting changes in the loss power across the separatrix $P_{Sep} = P_{in} - P_{Rad}$.

In pulse #96501, just prior to the increase in $\mathcal{F}_{Rad}$ at 9.5 s, there is a temporary drop in the NBI power by $\sim 5\,MW$ for ~ 0.3 s, after which there is a decrease in $T_{i,ped}$ and reduction in f_{ELM}, which can be explained by a reduction in P_{Sep} due to the increased radiated power and the power dependence of f_{ELM} for type-I ELMs. However, the behaviour of the optimised pulse #97781, in which the high-power heating is maintained, is quite different. Following the impurity accumulation at 9.5 s, the radiation fraction $\mathcal{F}_{Rad}$ decreases (due to the W impurities having a lower emissivity at the higher T_e prevalent in the core) and the consequent increase in P_{Sep} causes an increase in f_{ELM}.

The different ELM behaviour between the two cases is accompanied by changes to the normalised gradients across the pedestal, with $\langle R/L_{n_e}\rangle_{ped}$ slightly lower and both $\langle R/L_{T_i}\rangle_{ped}$ and $\langle R/L_{T_e}\rangle_{ped}$ slightly higher on average over this later phase. These changes combine to significantly increase
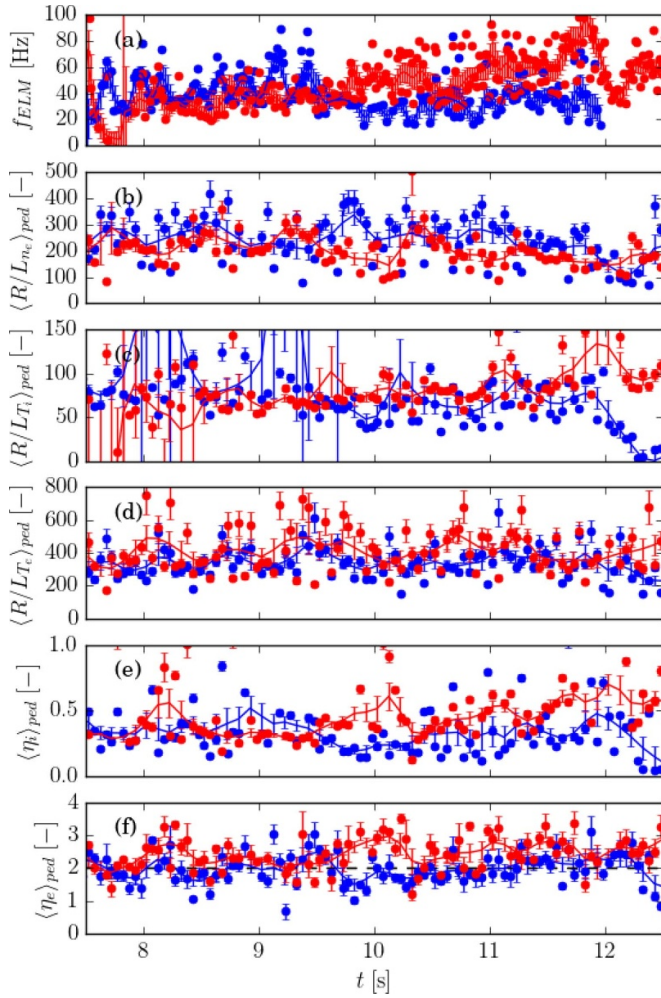
Figure 7. Evolution during the two hybrid pulses #96501 (black) and #97781 (red) of: the ELM frequency f_{ELM} (*a*), the normalised gradients $\langle R/L_{n_e}\rangle_{\mathrm{ped}}$ (*b*), $\langle R/L_{T_i}\rangle_{\mathrm{ped}}$ (*c*) and $\langle R/L_{T_e}\rangle_{\mathrm{ped}}$ (*d*) and the parameters $\langle \eta_i\rangle_{\mathrm{ped}}$ (*e*) and $\langle \eta_i\rangle_{\mathrm{ped}}$ (*f*) averaged over the pedestal region for the time period 7.5–12.5 s. The threshold $\eta_{i,cr}\sim 2$ is indicated by the dashed line.

Figure 8. Inter-ELM evolution of the parameters $\{\eta_i\}_{\mathrm{man}}^{\mathrm{max}}$ (*a*), (*b*) and $\langle \eta_i\rangle_{\mathrm{ped}}$ (blue) and $\langle \eta_e\rangle_{\mathrm{ped}}$ (red) (*c*), (*d*) averaged over the mantle and pedestal regions for the two hybrid pulses #96501 and #97781 for the time period 9.5–11.5 s. Data are at the times of the TS laser pulses plotted relative to the time of the previous ELM Δt_{ELM}. The threshold $\eta_{i,cr}\sim 2$ is indicated by the dashed line.

3.4.4. Inter-ELM dynamics of NC convection. The density losses caused by the ELMs change the gradients and hence the profiles of the derived parameters $\eta_{i,e}$ and $\zeta_{i,e}$ in the pedestal and mantle regions, which then evolve during the subsequent inter-ELM period. The HRTS measurements of the T_e and n_e profiles are essentially instantaneous at the laser pulse times, which are separated by 50 ms and occur at random times relative to the ELMs, Δt_{ELM}. Similarly, the CXRS measurements of the T_i profiles are available at an integration time of 10 ms at 100 Hz sample rate.

Hence, the kinetic profile data can be used to determine the inter-ELM evolution of the NC impurity screening across the pedestal and mantle regions. The inter-ELM evolution of the parameters $\{\eta_i\}_{\mathrm{man}}^{\mathrm{max}}$ and both $\langle \eta_i\rangle_{\mathrm{ped}}$ and $\langle \eta_e\rangle_{\mathrm{ped}}$ relative to the time of the ELM Δt_{ELM} are compared in figure 8 between the two hybrid pulses #96501 and #97781.

3.4.4.1. Mantle region. The ELM density losses reduce the pedestal density $n_{e,\mathrm{ped}}$ and hence increases the both the absolute and normalised density gradients n_e' and R/L_{n_e} across the mantle region just inside the pedestal top, resulting in a *decrease* of the parameter $\{\eta_i\}_{\mathrm{man}}^{\mathrm{max}}$ to ~ 2. As $n_{e,\mathrm{ped}}$ increases during the inter-ELM period, R/L_{n_e} decreases across the mantle and consequently $\{\eta_i\}_{\mathrm{man}}^{\mathrm{max}}$ increases to ~ 8 by the end of the ELM cycle. Hence, the NC impurity screening weakens after each ELM due to the stronger density gradient across the mantle and then strengthens again during the ELM cycle.

the values of $\langle \eta_i\rangle_{\mathrm{ped}}$ and $\langle \eta_e\rangle_{\mathrm{ped}}$, in the case of the latter causing the critical value $\eta_{i,cr}\sim 2$ for outward NC convection to be exceeded in the optimised pulse. Note that the maximum values of both η_i and η_e across the pedestal are a factor ~ 2 higher than the spatially averaged values.

If the temperature of the main D^+ ions across the pedestal were closer to T_e than to that of the Ne^{10+} impurity ions used for the CXRS measurements, then because $\langle \eta_e\rangle_{\mathrm{ped}} > \eta_{i,cr}$, it is possible that NC impurity screening across the pedestal gradient region is maintained throughout the later phase of the optimised pulse #97781 but is lost at the time of the NBI power drop in pulse #96501 due to a reduction of the pedestal T_i gradient. This highlights the necessity of sustained, high-power heating to maintain W impurity temperature gradient screening at the plasma periphery that is initially set up by optimising the gas fuelling.
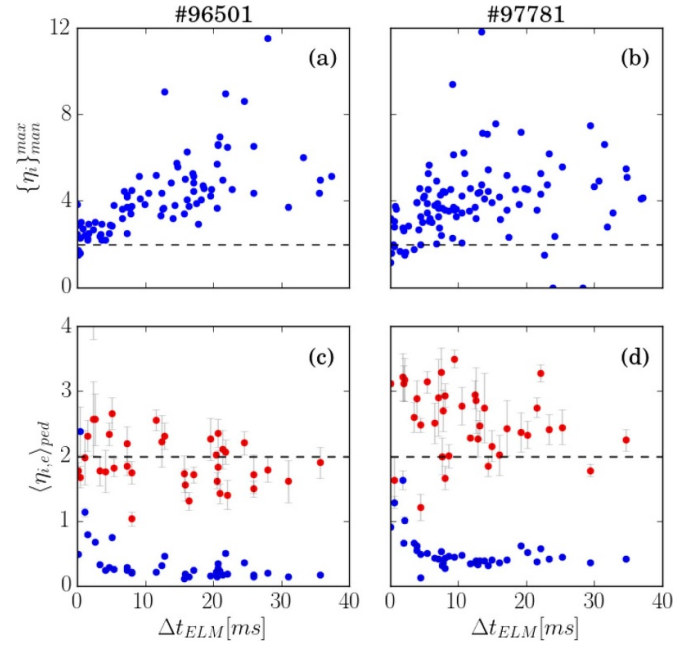
Consequently, a higher ELM frequency might be expected on average to reduce the impurity screening across the mantle region.

3.4.4.2. Pedestal region.

The inter-ELM dynamics of $\langle \eta_i \rangle_{\mathrm{ped}}$ for the pedestal region are the inverse of that for the mantle region, i.e. the decrease in $n_{e,\mathrm{ped}}$ due to the ELMs decreases R/L_{n_e} across the pedestal and hence *increases* $\langle \eta_i \rangle_{\mathrm{ped}}$ just after the ELMs. The subsequent increase of $n_{e,\mathrm{ped}}$ and hence decrease of R/L_{n_e} across the pedestal then causes $\langle \eta_i \rangle_{\mathrm{ped}}$ to decrease during the ELM cycle. As the values of $\langle \eta_i \rangle_{\mathrm{ped}} \sim 0.2 - 0.5 \ll \eta_{i,cr}$, the NC impurity convection across the pedestal is always expected to be strongly inward ($\langle \zeta_{\mathrm{NC},i} \rangle_{\mathrm{ped}} \ll 0$) in both pulses, consistent with the data in table 2, at least if it is the case that the edge CXRS measurements give the correct D^+ ion temperature in the pedestal region.

3.5. Numerical calculations of the W transport

Toroidal rotation affects the transport coefficients defined in equation (2) by modifying the poloidal distribution of the particle densities, particularly of the heavy impurities such as W. This introduces a further dependence on the toroidal Mach number M_ϕ as well as the parameters (g, Z_I, A_I, f_t). Note that the analytic model of Fajardo *et al* [15] has recently been extended to incorporate these dependencies. This will be the subject of a forthcoming publication [16], which will be of use for future interpretive analysis and predictive modelling.

Results from calculations performed using the drift-kinetic solver NEO for W^{28+} ions on a flux surface just inside the pedestal top ($\rho_{\mathrm{tor}} \sim 0.9$, where $f_t \sim 0.71$) of a JET-ILW equilibrium are presented in figure 9, which shows the dependencies of the enhancement of the impurity diffusion coefficient due to toroidal rotation $D_{\mathrm{NC,W}}(M_{\phi,I})/D_{\mathrm{NC,W}}(0)$ and of the temperature screening parameter C_{TS} on the collisionality parameter $g = \nu_{ii}^* \epsilon^{3/2}$ for various values of the generalised impurity Mach number $M_{\phi,\mathrm{W}}$.[9]

The primary effect of increased rotation is to increase all three transport coefficients (D_I, H_I, K_I) over their values without rotation, increasingly so over the collisionality range $10^{-3} < g < 10^{-2}$. However, the effect of rotation on the temperature screening parameter $C_{\mathrm{TS}} = -H_I/K_I$ is more complex, depending on whether the impurities are in the PS or BP regime. The magnitude of C_{TS} increases, both at low collisionality ($g \lesssim 10^{-3}$), where $C_{\mathrm{TS}} > 0$ and T_i' screens the impurities, and at high collisionality ($g \gtrsim 1$, not shown in figure 9), where $C_{\mathrm{TS}} < 0$ and T_i' enhances the impurity pinch. In the intermediate collisionality regime, the value of g where C_{TS} changes sign increases with $M_{\phi,I}$ and is also dependent on the other parameters (A_I, Z_I, f_t) and hence on the ion species and radial location within the plasma.
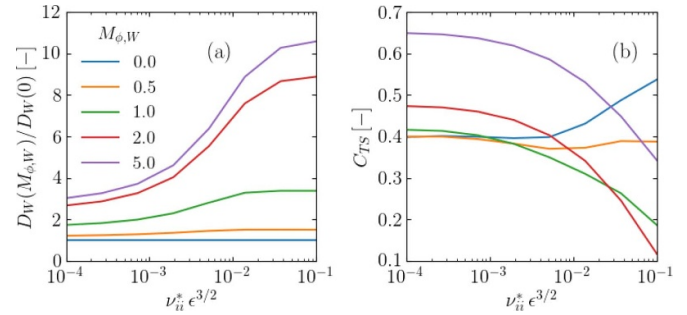

Figure 9. The dependence on the collisionality parameter $g = \nu_{ii}^* \epsilon^{3/2}$ of: (*a*) the ratio of the W diffusion coefficient calculated with rotation to that without $D_{\mathrm{NC,W}}(M_{\phi,I})/D_{\mathrm{NC,W}}(0)$ and (*b*) the temperature screening parameter C_{TS} for a range of values of the generalised impurity Mach number $M_{\phi,I}$ calculated using NEO for W^{28+} at the $\rho_{\mathrm{tor}} = 0.9$ flux surface of a JET-ILW equilibrium.

Hence, at low collisionality and high Mach number an operational window opens where the temperature screening of impurities is enhanced by increasing rotation, opposite to the impact of rotation at high collisionality [9]. Note that over the mantle and pedestal regions the screening parameter $C_{\mathrm{TS}} \sim 0.5$, except close to the separatrix where it decreases significantly. Hence, it is a valid assumption to assume this value of C_{TS} when calculating the screening parameter ζ_{NC} discussed in section 3.4 above.

3.5.1. Kinetic profile data.

An example of the raw and fitted kinetic profile data used for calculations of the NC W transport is shown in figure 10 for pulse #97781, averaged over a 1 s period of the post-accumulation phase from 10.5–11.5 s, where both the raw and fitted data are averaged separately, after performing separate fits to measurements at 50 ms intervals.[10] Both the raw n_e and T_e data from HRTS is measured at the laser repetition period of 50 ms and the CXRS T_i and Ω_ϕ data is measured with an integration period of 10 ms. Profiles measured during or immediately following ELMs are not included in the set of averaged profiles.

The profiles are fitted using a 3rd-order polynomial over the core and an mtanh() function [47] for the pedestal region, which is constrained to give zero value in the SOL. The requirement to fit the whole core profile with a rather stiff function is the reason why the fitted profiles depart from the measurements in some places. However, this does provide a reasonable interpolation between the measurements from the core and edge CXRS systems, the former giving higher values of T_i and Ω_ϕ than the edge system over the region where the measurements overlap. Note that only the edge CXRS data is used in the calculations of the NC convection parameter $\zeta_{\mathrm{NC},i}$ presented earlier.

It is striking that, over the steep-density gradient region of the pedestal, the measured T_i exceeds T_e, with a much weaker gradient and relatively high value ~ 1 keV at the separatrix,

---

[9] The generalised Mach number of the impurity ions is defined as $M_{\phi,I}^2 = \left[\frac{A_I}{A_i} - \frac{Z_I}{Z_i} \left(\frac{1}{(1+T_i/T_e)} \right) \right] M_{\phi,i}^2$.

[10] Note that the profiles must be plotted vs' $\rho_{\mathrm{pol}} \equiv (\psi_N)^{1/2}$ rather than ρ_{tor} because the toroidal flux is not defined outside the LCFS.
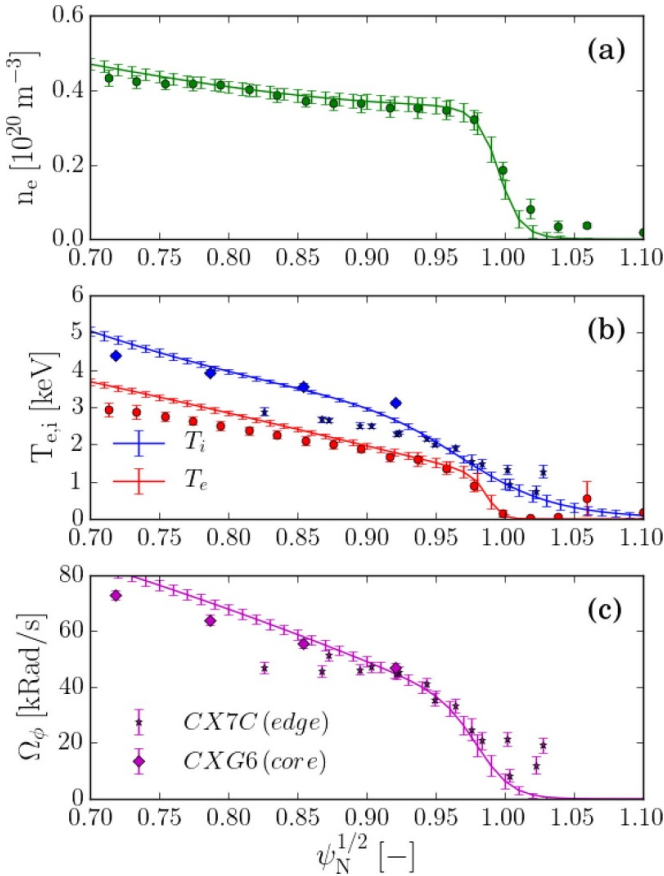
Figure 10. Profiles of n_e (*a*); T_e and T_i (*b*); Ω_ϕ (*c*) for the pulse #97781, where the fits (lines) and raw measurement data (points) from HRTS and the core and edge CXRS systems are both separately averaged over the 1 s time period 10.5–11.5 s.

where $T_e \sim 100$ eV. Also, the Ω_ϕ data is particularly not well represented by the mtanh() function in this region and the measured points are also non-monotonic.

There are several reasons why the CXRS measurements of T_i and Ω_ϕ over the pedestal region are challenging and it is particularly difficult to determine their gradients accurately, this affecting the derived values of η_i across this region:

- The rapidly decreasing Ne^{10+} density outwards across the pedestal results in lower CX line intensities for the T_i and Ω_ϕ measurements, making these less reliable and prone to contamination by small impurity lines towards and outside the separatrix.
- The off-mid-plane CXRS measurements (and to a lesser degree the HRTS measurements) require mapping to the magnetic axis by means of the magnetic equilibrium to be able to align them to calculate the profile of η_i across the pedestal. This requires using a pressure-constrained EFIT equilibrium (EFTP) with well-defined separatrix location, which uses the separatrix temperature $T_{e,\text{sep}} \sim 100$ eV as an additional constraint in the reconstruction.
- Fast EFIT equilibrium reconstructions or flux measurements show that there are small movements of the separatrix location by 1–2 cm during the ELM cycle due to changes in β_p
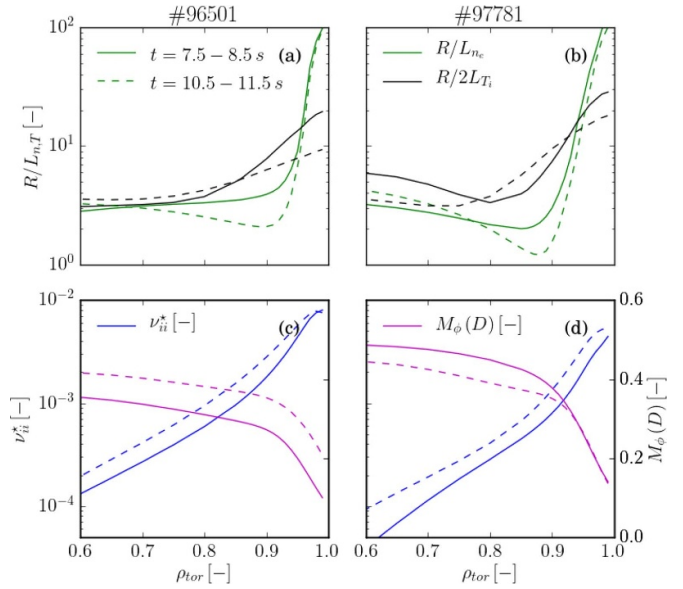

Figure 11. Profiles of parameters input to NEO vs' normalised radius ρ_{tor} for the two pulses #96501 and #97781: (*a*), (*b*) the normalised gradients R/L_{n_i} (green) and $R/2L_{T_i}$ (black); (*c*), (*d*) ion collisionality ν_{ii}^* (blue) and Mach number of the D^+ ions $M_\phi(D^+)$ (magenta), averaged over the time periods 7.5–8.5 s (solid) and 10.5–11.5 s (dashed).

during the ELM cycle, which imposes an intrinsic limitation on the accuracy of the mapping, which uses the EFTP equilibrium available with lower time resolution.

- As discussed earlier, on devices with a main ion (D^+) CXRS system, e.g. DIII-D, it is often found that over the pedestal region the ion-temperature T_i is closer to T_e than that measured on the impurity ions (i.e. C^{6+} on DIII-D or Ne^{10+} on JET-ILW) [45]. Without main-ion CXRS measurements in the pedestal region, there is no way to determine whether this is also the case under these conditions on JET-ILW.

3.5.2. Calculation of the W transport coefficients. Profiles of the parameters used to perform the NEO calculations are shown in figure 11 for the two pulses #96501 and #97781. As the temperature screening parameter $C_{\text{TS}} \sim 0.5$ across the full profile, in the case of the normalised temperature gradient $R/2L_{T_i}$ is shown for comparison with R/L_{n_i} because where the $R/2L_{T_i} \gtrsim R/L_{n_i}$ impurity screening is expected.

Just inside the top of the pedestal[11], at $\rho_{\text{tor}} \sim 0.9$ the toroidal Mach number of the D^+ ions $M_\phi(D) \sim 0.3$ in pulse #96501, which corresponds to a Mach number $M_{\phi,I} \sim 2.4$ for the highly charged W^{28+} ions, while in the optimised pulse #97781 these values are a factor ~ 1.3 higher. The collisionality of the D^+ ions is in the range $10^{-4} < \nu_{ii}^* < 10^{-2}$, i.e. in the collisionless banana regime.

Profiles of η_i and values of the inverse screening parameter $1/C_{\text{TS}}$ are shown in figure 12, so that regions where impurity screening is expected (where $\eta_i > \eta_{i,cr} = 1/C_{\text{TS}} \sim 2$) can be discerned, i.e. in particular across the mantle region

---

[11] The top of the density pedestal is located at $\rho_{\text{tor}} \sim 0.95$.
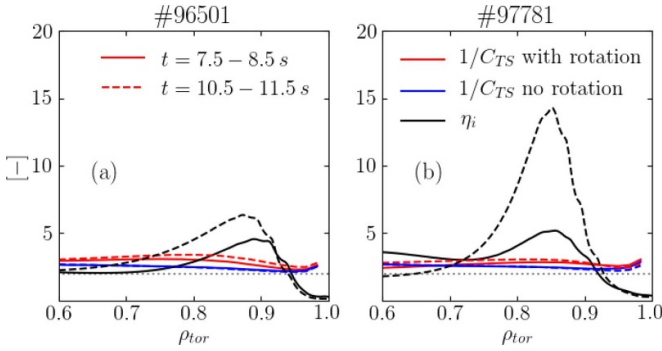
Figure 12. Profiles of the parameter η_i (black) and the inverse of the impurity screening parameter $1/C_{TS}$ vs' normalised radius ρ_{tor} calculated using NEO for the input profiles shown in figure 11 for the two pulses #96501 (*a*) and #97781 (*b*), averaged over the time periods 7.5–8.5 s (solid) and 10.5–11.5 s (dashed).

$(0.8 \lesssim \rho_{tor} \lesssim 0.95)$ inside the pedestal top, whereas in the pedestal region strong, inward impurity convection is expected.

Profiles of the calculated W diffusion coefficient $D_{NC,W}$ and of the NC convection velocity $V_{NC,W}$ for the W ions are shown in figure 13 for the pulses #96501 and #97781. Profiles calculated both with and without rotation show that the NBI-driven toroidal rotation enhances the impurity transport by $\sim \mathcal{O}(10)$ above the level for a non-rotating plasma. Furthermore, the higher Mach number $M_{\phi,i}$ early on in the optimised pulse #97781 enhances W transport coefficients, increasing $D_{NC,W}$ in the mantle region, by a factor ~ 1.5 at $\rho_{tor} \sim 0.9$ compared to that in pulse #96501. This enhancement also increases the outward W convection velocity $V_{NC,W}$ by a similar factor.

The resulting values of $D_{NC,W}$ and $V_{NC,W}$ can be used to calculate the W density profile, both as a FSA quantity $\langle n_W \rangle$ and across the LFS major radius through the magnetic axis $n_W(R)$, as described below. These are used to calculate the total corresponding emissivity profile of the W impurities $\epsilon_{tot,W}$, which are then compared with the total emissivity ϵ_{tot} derived from bolometric measurements.

3.5.3. Calculation of the W density and emissivity profiles. The density profile of the W impurities is calculated following the approach described in [48]. In steady-state conditions, in the core plasma there is an absence of impurity sources and sinks. Hence, simplifying the notation for the FSA, the continuity equation for the impurities $\nabla \cdot (\Gamma_W) = 0$ implies that everywhere the W flux $\Gamma_W = 0$.[12]

Neglecting the contributions to the W transport from NC diffusion and the anomalous turbulent pinch, i.e. assuming $D_{an,W} \gg D_{NC,W}$ and $V_{NC,W} \gg V_{an,W}$ (where D_{an} and V_{an} are the turbulent impurity diffusivity and convective pinch velocity), the W flux is given by $\Gamma_W = V_{NC,W} n_W - D_{an,W} n'_W$. Hence, the logarithmic W density gradient can be

---

[12] Note that it is not necessary to model the transport of each ionisation stage of the impurities separately because the relevant atomic rate coefficient used to calculate the total emissivity $\mathcal{R}_\epsilon$ is available for a 'bundled' ensemble of ions at the appropriate fractional abundances for the impurities in coronal equilibrium [37].
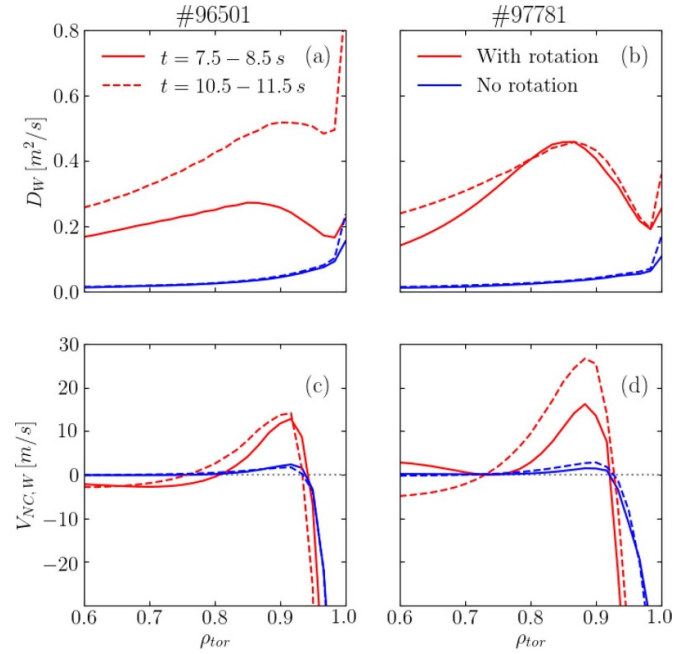

Figure 13. Profiles of the NC W convection velocity $V_{NC,W}$ vs' normalised radius ρ_{tor} calculated using NEO for the input profiles shown in figure 11 for the two pulses #96501 (*a*) and #97781 (*b*), averaged over the time periods 7.5–8.5 s (solid) and 10.5–11.5 s (dashed).

expressed as $\ln(n_W)' = V_{NC,W}/D_{an,W}$, where the $' \equiv d/dr$. It is then straightforward to integrate this expression radially, taking the boundary condition as the value of n_W either at the magnetic axis or separatrix, to yield the W density profile across the LFS mid-plane, where the poloidal angle $\theta = 0$:

$$n_W(R, \theta = 0) = \exp \left\{ \int \left(\frac{V_{NC,W}}{D_{an,W}} \right) dR \right\}. \quad (3)$$

For calculation of the FSA W density, it is necessary to know its dependence on the poloidal location around the flux surface, i.e. $n_W(r, \theta)$, where r is a suitable flux-surface label, e.g. ρ_{tor}. The centrifugal force acting on the heavy impurities due to toroidal rotation concentrates their densities at the LFS of the plasma [34], with their density distribution given by equation 6 of [48]:

$$\frac{n_W(R, \theta)}{n_{W,0}}$$
$$= \exp \left\{ -\frac{Z_I e \Phi(r, \theta)}{T_i(r)} + \frac{m_I \Omega_\phi(r)^2}{2 T_i(r)} \left(R(r, \theta)^2 - R_0(r)^2 \right) \right\} \quad (4)$$

where $\Phi(r, \theta)$ is the calculated electrostatic potential and $R_0(r) = R(r, \theta = 0)$. The FSA density $\langle n_W \rangle$ can then be calculated in the usual way.[13]

---

[13] The flux-surface average of a quantity X is defined as $\langle X \rangle = \oint X \frac{dl_p}{B_p} / \oint \frac{dl_p}{B_p}$, where B_p is the poloidal component of the magnetic field and l_p is the path length around the flux surface in a plane of constant toroidal angle.
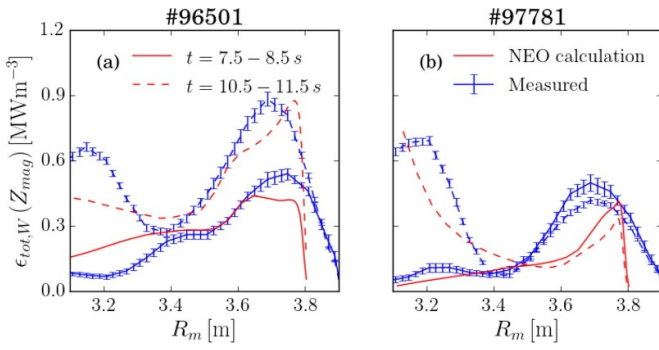
Figure 14. Total emissivity profiles across the LFS mid-plane (@ $Z = Z_{\text{mag}}$) vs major radius R determined from tomographic reconstructions of the bolometric data (blue) and calculated using the NC transport coefficients from NEO (red) for the two pulses #96501 (*a*) and #97781 (*b*) for the time periods 7.5–8.5 s (solid) and 10.5–11.5 s (dashed).

Figure 15. FSA total emissivity profiles $\langle \epsilon_{\text{tot}} \rangle$ vs normalised radius ρ_{tor} determined from tomographic reconstructions of the bolometric data (blue) and calculated using the NC transport coefficients from NEO (red) for the two pulses #96501 (*a*) and #97781 (*b*) for the time periods 7.5–8.5 s (solid) and 10.5–11.5 s (dashed).

For calculation of the anomalous turbulent impurity diffusivity $D_{\text{an,W}}$, this is assumed to be equal to that of the background D^+ ions D_{an},[14] where an expression for mixed Bohm/gyro-Bohm transport is used [49], as described in [50].

For comparison with data from tomographic reconstructions, e.g. as shown in figure 2, total emissivity coefficients $\mathcal{R}_\epsilon(T_e, n_e)$ for W impurities in coronal equilibrium from the ADAS atomic database [37] are used to calculate the total emissivity of the W ions, $\epsilon_{\text{tot,W}}(r) = n_{\text{W}}(r)\mathcal{R}_\epsilon(r)$. Note that because the electron temperature is a flux function $T_e(\psi_{\text{N}})$, either the FSA profile or LFS profile of $\epsilon_{\text{tot,W}}$ can be calculated using the appropriate density profile, $n_{\text{W}}(R)$ or $\langle n_{\text{W}} \rangle(r)$.

3.5.4. Comparison of total emissivity profiles. Profiles of the measured total emissivity across the LFS mid-plane, through the magnetic axis ($Z = Z_{\text{mag}}$) determined from tomographic reconstructions of the bolometer data are compared to the calculated emissivity profiles in figure 14 for the two pulses #96501 and #97781. The profiles are averaged over two 1 s time ranges during the early phase (7.5–8.5 s) and later (10.5–11.5 s), after the W has accumulated in the plasma core. Because only the relative emissivity profiles can be calculated without knowledge of the W influx, the calculated profiles are normalised to the measured values at $R = 3.5$ m.

For pulse #96501, the shape of the ϵ_{tot} profiles are reasonably well reproduced using the transport coefficients from NEO[15]. Outside the separatrix ($R_{\text{sep}} \sim 3.8$ m), $\epsilon_{\text{tot,W}}$ is not calculated, while the measured profile may be broadened somewhat into the SOL due to the finite spatial resolution ($\delta R \sim$ 0.05–0.1 m) of the measurement and reconstruction.

In the case of pulse #97781, over the mantle region, the calculated $\epsilon_{\text{tot,W}}$ profiles are hollow, consistent with the outward NC convection. The increasing gradient towards the periphery can be ascribed to a local overestimation of the NC convection $V_{\text{NC,W}}$ or more likely an underestimate of the anomalous diffusivity $D_{\text{an,W}}$. The accumulation of the W at the later time period is well reproduced by the calculation in this pulse. Note that, at the later time, whereas the emission from the core plasma is similar between the two pulses, the emissivity from the mantle region is almost a factor ~ 2 higher in the non-optimised pulse #96501.

The $\langle \epsilon_{\text{tot}} \rangle$ profiles in figure 15 show that the radiation from the mantle region is far less significant in a FSA sense compared to that from the LFS mid-plane where the W is localised by the toroidal rotation. However, the larger volume of this region compared to the core ($r/a < 0.3$) results in $\sim 50\%$ of the radiated power being emitted from impurities in the mantle, while only $\sim 30\%$ is emitted from the core. Note that both the calculated and measured $\langle \epsilon_{\text{tot}} \rangle$ profiles are consistent with significant localisation of the W impurities close to the separatrix due to the outward NC convection.

Although FSA data is not available outside of the separatrix ($r/a > 1$), the LFS profiles in figure 14 show that there is significant emission from impurities the SOL region. The 2D distributions in figure 2 show that the radiation from the pedestal foot and SOL is dominated by emission from the region above the HFS divertor leg. Strong emission from this region is frequently observed in high-power H-mode pulses in JET-ILW and has been attributed to the poloidal localisation of impurities to a so-called HFS high-density (HFSHD) region [51]. The significance of this will be discussed in section 4 below.

4. Summary and conclusions

4.1. Evidence for high-Z impurity screening

Reduced gas fuelling during the initial H-mode phase of the optimised hybrid pulse #97781 results in both significantly higher ($\sim \times 2$) ion temperature $T_{i,\text{ped}}$ and toroidal rotation at

---

[14] Note that because the anomalous transport is expected to be due to electrostatic turbulence, the associated transport due to fluctuating $\tilde{E} \times B$ drifts is the same for all particle species, independent of charge and mass [38].

[15] As mentioned previously, it is a good approximation in high-power JET-ILW pulses that radiation from W impurities dominate the total emissivity.
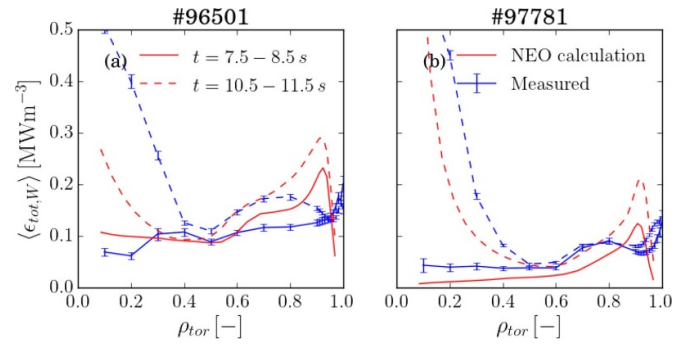
the pedestal top $\Omega_{\phi,\mathrm{ped}}$, particularly early in the pulse, although the enhancement persists later into the steady ELMy H-mode phase. The effect of the strong toroidal rotation ($M_\phi(D^+) \sim \mathcal{O}(0.4)$) is to localise the heavy impurities to the LFS mid-plane, thereby enhancing the level of collisional NC transport by $\mathcal{O}(10)$.

During the initial phase, before the W impurities accumulate in the core, analysis of the fast bolometry signals reveals that in the optimised pulse, there is a reduction in changes to the relative W content of the plasma $\Delta \bar{n}_\mathrm{W}/\bar{n}_\mathrm{W}$ due both the ELM flushing and inter-ELM ingress of these impurities relative to those in the non-optimised pulse. This indicates that the influx of W across the pedestal is already reduced during this early phase.

Calculations using NEO of the NC transport of the W impurities using measured ELM-averaged kinetic profiles, reveals that there is certainly screening due to outward convection ($V_\mathrm{NC,W} > 0$) in the mantle region, just inside the pedestal top in both of the pulses compared here. This screening, which occurs when $\eta_i > 1/C_\mathrm{TS} \sim 2$, is enhanced by the $\sim \times 1.5$ stronger toroidal rotation at the pedestal top in the optimised compared to the non-optimised pulse.

Note that calculations with ASTRA [52] for Q = 10 ITER plasmas [53], consistent with evaluations of turbulent transport and intrinsic torque [54], predict reduced toroidal Mach number of the D^+ ions $M_{\varphi,\mathrm{I}}$ at the pedestal top of ~ 0.11,[16] which is considerably lower than the values of $\sim 0.3 - 0.4$ for the hybrid-scenario plasmas discussed here. As discussed in [16], the current expectation of low rotation in ITER implies that it will likely not significantly profit from rotation-enhanced W screening across the mantle region, although W screening is expected to occur across the pedestal gradient region [55].

As evident from the FSA emissivity profiles, the presence of less W in the mantle only partly explains why the ELMs flush less W from the confined plasma in the optimised pulse—the factor ~ 2 reduction in $\langle \epsilon_\mathrm{tot} \rangle$ is less than the decrease in the W flushing efficiency $(\Delta \bar{n}_\mathrm{W}/\bar{n}_\mathrm{W})_\mathrm{ELM}$ and also of the corresponding inter-ELM influx. Although after the initial phase ($t > 8$ s), the gas fuelling is the same in both pulses, differences in their behaviour persist, i.e. the higher $T_{i,\mathrm{ped}}$ and $\Omega_{\phi,\mathrm{ped}}$ in the optimised pulse (both enhancing impurity screening) and also in the radiation and ELM behaviour.

After the W accumulates in the plasma core, in the non-optimised pulse, following a temporary drop in the NBI heating power, the radiated power fraction $\mathcal{F}_\mathrm{Rad}$ increases significantly. The resulting reduction in the loss power P_Sep across the pedestal causes both the ELM frequency f_ELM and also $T_{i,\mathrm{ped}}$ to decrease, which consequently reduces the peripheral impurity screening. This results in a loss of performance in terms of energy confinement and neutron rate due to the higher radiated power and lower core temperature. This observation highlights the importance of sustained high-power heating in

maintaining the temperature-gradient impurity screening at the plasma periphery.

The inter-ELM dynamics of the impurity screening caused by the ELM density losses exhibit opposite trends for the convection across the pedestal gradient region and the mantle. Just after the ELMs, temperature screening across the mantle is reduced by lower $\langle \eta_i \rangle_\mathrm{man}$, while inward convection across the pedestal is reduced by a higher $\langle \eta_i \rangle_\mathrm{ped}$, so these effects partially compensate from the point of view of the net influx.

ELM flushing results from the fast bolometry exhibit a reversal of the typical situation during the later phase of the optimised pulse, i.e. instead of the ELMs flushing W from the plasma, on average they slightly increase the W content of the plasma (by $\lesssim 1\%$), which is then expelled between the ELMs rather than entering the confined plasma. This observation, together with the fact that $\mathcal{F}_\mathrm{Rad}$ remains controlled, indicates that during this later phase: (a) there is efficient impurity screening at the pedestal, resulting in a hollow impurity density profile across the pedestal; (b) this has the consequence that ELMs can transport impurities into the confined plasma rather than flush them out, as originally identified in simulations performed for ITER [7, 56].

Using the available ion temperature measurements from the edge CXRS system, it has not been possible to confirm the presence of NC temperature-gradient impurity screening across the steep-density gradient region of the pedestal by modelling of the NC transport. However, it is possible that, were the D^+ ion temperature gradient across the pedestal to be higher than that of the impurities, such screening may also be present across the steep gradient region—assuming that $T_i = T_e$ across the pedestal does result in sufficiently high $\eta_i = \eta_e > 2$ for screening. Without a measurement of the D^+ temperature, there is no way to be sure but the other results presented here are consistent with this conjecture.

The observation that ELMs can cause an ingress of impurities into the confined plasma is probably due to an interchange nature to this explosive instability [22],[17] rather than a reversal of the collisional NC transport during the ELMs. If the impurity content of the outer pedestal/SOL plasma is higher than that in the mantle region, just inside the pedestal top, the ELMs can cause a net increase in the impurity content of the confined plasma, a fact which has consequences for the operation of ITER.

During the recent JET-ILW DT campaign (DTE2) at the end of 2021, this hybrid scenario was used to run the best performing DT pulse #99950 with a record fusion energy of 45.8 MJ and power averaged over 5 s of 8.3 MW [58], albeit with slightly modified gas fuelling to account for the slower response of the tritium injection module and increased particle confinement in DT compared to D plasmas. Both this pulse and the D pulse #100822, with matched engineering parameters,

---

[16] The most relevant rotation profiles for ITER Q = 10 plasmas shown in figure 1 of [53] are those for a case with Prandtl number $\mathrm{Pr} \equiv \chi_\varphi/\chi_i = 0.3$ and ratio of momentum to energy confinement times $\tau_\varphi/\tau_\mathrm{E,th} = 2$ with pedestal top rotation $\Omega_{\varphi,\mathrm{ped}} \sim 10$ krad/s, corresponding to $M_{\varphi,\mathrm{I}} \sim 0.11$ with $T_{i,\mathrm{ped}} \sim 4.2$ keV.

[17] The interchange nature of ELMs has been demonstrated by means of fast beam-emission spectroscopy (BES) measurements of the edge density profile on MAST [57].

exhibited similarly high edge T_i and reduced edge radiation as in the optimised D pulse #97781 discussed in detail here.

4.2. Significance for ITER operation

Since the effect of NC temperature gradient screening scales with impurity charge Z, it is stronger for W relative to turbulent impurity transport than for lower Z impurities and so easier to detect. Furthermore, this empirical confirmation of this phenomenon relies on bolometric measurements of $P_{\mathrm{Rad}}^{\mathrm{Pl}}$ rather than spectroscopy, which is very difficult for W. The concomitant observation that ELMs allow W back into the plasma, in optimised high-power hybrid-scenario pulses on JET-ILW is important for several reasons:

Firstly, scenarios that integrate core fusion performance, i.e. high fusion gain Q, and tolerable inter-ELM divertor power loads automatically require a high separatrix to pedestal density ratio $n_{e,\mathrm{sep}}/n_{e,\mathrm{ped}} \gtrsim 0.4$, resulting in W pedestal screening [55]. However, with inter-ELM W screening, the requirements for ELM control and W efflux are orthogonal, which questions whether active triggering of the ELMs for their control can be solution to the ELM problem.

If W brought into the plasma by ELMs (as predicted in [22]), and only expelled between them, then increasing the ELM frequency f_{ELM} will increase $\mathcal{F}_{\mathrm{Rad}}$, eventually causing an H/L transition [7]. Furthermore, a weak decrease of the ELM target heat flux is expected with increasing f_{ELM}. Hence, increasing f_{ELM} cannot give a consistent solution to the power flux and W contamination problem in the presence of W screening [56].

This conundrum does not occur in ITER-baseline scenario pulses, in which W is localised to the mantle and hence power and impurity exhaust go together [12], as was assumed when the original ELM control requirements for ITER were derived [59]. Hence, these new JET results justify that ELM suppression rather than mitigation by controlled ELM triggering is the preferred solution for ITER, since it can provide the solution to the power exhaust problem and, together with W pedestal screening, good W impurity exhaust. However, a disadvantage of this strategy for use in a future fusion reactor, is that fuelling of the confined plasma with extrinsic impurities, e.g. the noble gas Ar, as a means of mitigating the power exhaust problem would be ineffective.

Acknowledgments

ORCID iDs

A.R. Field ⓘ https://orcid.org/0000-0003-0671-9668
F.J. Casson ⓘ https://orcid.org/0000-0001-5371-5876
D. Fajardo ⓘ https://orcid.org/0000-0001-5802-4572
C. Angioni ⓘ https://orcid.org/0000-0003-0270-9630
J. Hobirk ⓘ https://orcid.org/0000-0001-6605-0068
A. Kappatou ⓘ https://orcid.org/0000-0003-3341-1909
A. Loarte ⓘ https://orcid.org/0000-0001-9592-1117

References

[1] Matthews G.F. *et al* 2011 *Phys. Scr.* **T145** 014001
[2] Bigot B. *et al* 2019 *Nucl. Fusion* **59** 112001
[3] Naujoks D. *et al* 1996 *Nucl. Fusion* **36** 671
[4] Lawson J.D. 1955 *Proc. Phys. Soc.* B **70** 6–10
[5] Lux H. *et al* 2014 Radiation modelling in DEMO systems studies *ADAS Workshop* (*Warsaw, Poland*, *28–30 September 2014*) (available at: www.adas.ac.uk/2014talks/2014_ADAS-HLux.pdf)
[6] Pütterich T., Fable E., Dux R., O'Mullane M., Neu R. and Siccinio M. 2019 *Nucl. Fusion* **59** 056013
[7] Dux R., Loarte A., Angioni C., Coster D., Fable E. and Kallenbach A. 2017 *Nucl. Mater. Energy* **12** 28–35
[8] Hirshman S.P. and Sigmar D.J. 1981 *Nucl. Fusion* **21** 1079
[9] Angioni C. 2021 *Plasma Phys. Control. Fusion* **63** 073001
[10] Garcia J. *et al* 2021 Integrated scenario development at JET for DT operation and ITER risk mitigation *8th IAEA FEC* (*Nice, France*, *10–15 May 2021*) (available at: https://conferences.iaea.org/event/214/contributions/17020/attachments/10339/14604/IAEA_talk_jeronimo.pdf)
[11] Mailloux J. *et al* 2022 *Nucl. Fusion* **62** 042026
[12] Field A.R. *et al* 2021 *Plasma Phys. Control. Fusion* **63** 095013
[13] Pucella G. *et al* 2021 *Nucl. Fusion* **61** 046020
[14] Garcia J. *et al* 2022 *Phys. Plasmas* **29** 032505
[15] Fajardo D., Angioni C., Maget P. and Manas P. 2022 *Plasma Phys. Control. Fusion* **64** 055017
[16] Fajardo D. *et al* 2022 Model for the collisional transport in tokamaks and the combined impact of rotation and collisionality *26th US-EU TTF Meeting* (*Santa Rosa, California, USA*, *5–8 April 2022*) (available at: https://sites.google.com/ucsd.edu/ttf-2022/home?pli=1)
[17] Lee H., Lee H., Han Y.S., Song J., Belli E.A., Choe W., Kang J., Lee J., Candy J. and Lee J. 2022 *Phys. Plasmas* **29** 022504
[18] Belli E.A. and Candy J. 2008 *Plasma Phys. Control. Fusion* **50** 095010
[19] Belli E.A. and Candy J. 2009 *Plasma Phys. Control. Fusion* **51** 075018
[20] Belli E.A. and Candy J. 2012 *Plasma Phys. Control. Fusion* **54** 015015
[21] Huber A. *et al* 2007 *Fusion Eng. Design* **82** 1327–34
[22] van Vugt D.C., Huijsmans G.T.A., Hoelzl M. and Loarte A. 2019 *Phys. Plasmas* **26** 042508
[23] Czarny O. and Huysmans G. 2008 *J. Comput. Phys.* **227** 7423
[24] Garzotti L. *et al* 2019 *Nucl. Fusion* **59** 076037
[25] Kim S.H., Bulmer R.H., Campbell D.J., Casper T.A., LoDestro L.L., Meyer W.H., Pearlstein L.D. and Snipes J.A. 2016 *Nucl. Fusion* **56** 126002
[26] Kallenbach A., Beurskens M.N.A., Korotkov A., Lomas P., Suttrop W., Charlet M., McDonald D.C., Milani F., Rapp J. and Stamp M. (EFDA-JET Workprogramme Contributors and ASDEX Upgrade Team) 2002 *Nucl. Fusion* **42** 1184

[27] Andrew Y. and Hawkes N.C. 2006 *Rev. Sci. Instrum.* **77** 10E913

[28] Bartiromo R., Bombarda F., Giannella R., Mantovani S., Panaccione L. and Pizzicaroli G. 1989 *Rev. Sci. Instrum.* **60** 237

[29] Höbirk J. *et al* 2012 *Plasma Phys. Control. Fusion* **54** 195001

[30] Garbet X. *et al* 2004 *Plasma Phys. Control. Fusion* **46** B557

[31] Ingesson L.C., Alper B., Chen H., Edwards A.W., Fehmers G.C., Fuchs J.C., Giannella R., Gill R.D., Lauro-Taroni L. and Romanelli M. 1998 *Nucl. Fusion* **38** 11 1675

[32] Reimold F., Wischmeier M., Potzel S., Guimarais L., Reiter D., Bernert M., Dunne M. and Lunt T. 2017 *Nucl. Mater. Energy* **12** 193–9

[33] Field A.R. *et al* 2020 *Plasma Phys. Control. Fusion* **62** 055010

[34] Wesson J.A. *et al* 1997 *Nucl. Fusion* **37** 578

[35] Sertoli M., Flanagan J., Maslov M., Maggi C., Coffey I., Giroud C., Menmuir S., Carvalho P., Shaw A. and Delabie E. 2018 *Rev. Sci. Instrum.* **89** 113501

[36] Fedorczak N. *et al* 2015 *J. Nucl. Mater.* **463** 85–90

[37] Henderson S.S., Bluteau M., Foster A., Giunta A., O'Mullane M.G., Pütterich T. and Summers H.P. 2017 *Plasma Phys. Control. Fusion* **59** 055010

[38] Fussmann G., Field A.R., Kallenbach A., Krieger K. and Steuer K.H. (The ASDEX Team) 1991 *Plasma Phys. Control. Fusion* **33** 1677

[39] Lerche E. *et al* 2016 *Nucl. Fusion* **56** 036022

[40] Casson F.J. *et al* 2015 *Plasma Phys. Control. Fusion* **57** 014031

[41] Hender T.C. *et al* 2016 *Nucl. Fusion* **56** 066022

[42] Angioni C. and Helander P. 2014 *Plasma Phys. Control. Fusion* **56** 124001

[43] Helander P. and Sigmar D.J. 2002 *Collisional Transport in Magnetised Plasmas* 1st edn (Cambridge: Cambridge University Press)

[44] Pasqualotto R., Nielsen P., Gowers C., Beurskens M., Kempenaars M., Carlstrom T. and Johnson D. 2004 *Rev. Sci. Instrum.* **75** 3891–3

[45] Haskey S.R. *et al* 2018 *Plasma Phys. Control. Fusion* **60** 105001

[46] Weisen H., Delabie E., Flanagan J., Giroud C., Maslov M., Menmuir S., Patel A., Scott S., Siren P. and Varje J. 2020 *Nucl. Fusion* **60** 036004

[47] Dickinson D., Saarelma S., Scannell R., Kirk A., Roach C.M. and Wilson H.R. 2011 *Plasma Phys. Control. Fusion* **53** 115010

[48] Angioni C. *et al* 2014 *Nucl. Fusion* **54** 083028

[49] Erba M., Cherubini A., Parail V.V., Springmann E. and Taroni A. 1997 *Plasma Phys. Control. Fusion* **39** 261

[50] Casson F.J. *et al* 2020 *Nucl. Fusion* **60** 066029

[51] Potzel S. *et al* 2015 *J. Nucl. Mater.* **463** 541–5

[52] Polevoi A., Loarte A., Kukushkin A., Pacher H., Pacher G. and Köchl F. 2017 Analysis of fuelling requirements in ITER H-modes with SOLPS-EPED1 derived scalings *Nucl. Fusion* **57** 022014

[53] Li L., Liu Y., Loarte A., Pinches S., Polevoi A., Liang Y. and Zhong F. 2019 Modeling 3D plasma boundary corrugation and tailoring toroidal torque profiles with resonant magnetic perturbation fields in ITER *Nucl. Fusion* **59** 096038

[54] Chrystal C., Grierson B.A, Staebler G.M, Petty C.C, Solomon W.M, deGrassie J.S, Burrell K.H, Tala T. and Salmi A. 2017 Predicting rotation for ITER via studies of intrinsic torque and momentum transport in DIII-D *Phys. Plasmas* **24** 056113

[55] Dux R., Loarte A., Fable E. and Kukushkin A. 2014 *Plasma Phys. Control. Fusion* **56** 124003

[56] Polevoi A.R., Loarte A., Dux R., Eich T., Fable E., Coster D., Maruyama S., Medvedev S.Y., Köchl F. and Zhogolev V.E. 2018 *Nucl. Fusion* **58** 056020

[57] Valovič M., Garzotti L., Gurl C., Kirk A., Dunai D., Field A.R., Lupelli I., Naylor G. and Thornton A. (The MAST Team) 2015 *Nucl. Fusion* **55** 013011

[58] Kappatou A. *et al* 2022 Sustained high DT fusion power production with the hybrid scenario in the JET-ILW DTE2 campaign 64th Annual Conf. APD DPP (*Spokane, Washington State, USA*, *17–21 October 2022*) (available at: https://engage.aps.org/dpp/meetings/annual-meeting)

[59] Loarte A. *et al* 2016 *Nucl. Fusion* **54** 033007